International Journal of Machine Tools & Manufacture 189 (2023) 104030

Contents lists available at ScienceDirect

International Journal of Machine Tools and Manufacture

journal homepage: www.elsevier.com/locate/ijmactool

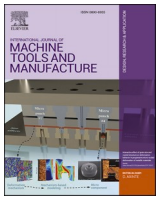

Research Paper

Analysis of burr formation in finish machining of nickel-based superalloy with worn tools using micro-scale in-situ techniques

Hamzah Zannoun [a,b], Julius Schoop [a,b,*]

[a] Institute for Sustainable Manufacturing, University of Kentucky, Lexington, KY, USA
[b] Department of Mechanical & Aerospace Engineering, University of Kentucky, Lexington, KY, USA

ARTICLE INFO

Handling Editor: Dragos Axinte

Keywords:
Burr formation
Inconel 718
Machining
Tool-wear
In-situ characterization
Digital image correlation (DIC)

ABSTRACT

The formation of burrs is among the most significant factors affecting quality and productivity in machining. Burrs are a negative byproduct of machining processes that are difficult to avoid because of a limited understanding of the complex burr formation mechanisms in relation to cutting conditions, including both process parameters and tool condition. Thus, the objective of this work was to characterize burr formation under finish machining conditions via a high-speed, high-resolution in-situ experimental method. Various parameters pertaining to burr geometry such as height, thickness, and initial negative shear angle were measured both during and after cutting. Results showed that varying the conditions of uncut chip thickness, tool-wear, and cutting speed all have a significant effect on burr formation, although certain burr metrics were found to be insensitive with respect to different process conditions because the difference was statistically insignificant. This study provides new insights into the relationships between the workpiece material's microstructure, machining parameters, and tool condition on both crack formation and propagation/plasticity during burr formation. Using digital image correlation (DIC) and a physics-based process model not previously utilized for burr formation analysis, the displacement and corresponding flow stress were calculated at the exit burr root location. This novel semi-analytical approach revealed that the normalized stress at the exit burr root was approximately equal to the flow stress for a variety of different conditions, indicating the potential for model-based prediction of burr formation mechanics. Finally, this study investigates factors that influence fracture evolution during exit burr formation. It was found that negative exit burrs are a direct result of high strain rate and high uncut chip thickness, which was expected, but also a microstructural size effect and a tool-wear effect, neither of which have been previously reported. By harnessing ultra-high-speed imaging and advanced optical microscopy techniques, this manuscript deals with the fundamentals of burr formation, including new insights into material response at the grain-scale to the loads imposed with both sharp and worn tools.

1. Introduction

Burr formation is among the most troublesome byproducts of machining processes. Burrs can be defined as material that plastically deforms around geometric discontinuities on a machining workpiece, such as exits, edges, and corners [1]. Burrs are very problematic for several reasons: they can act as stress risers and harm the fatigue life of components, ruin dimensional tolerances, and injure operators during the assembly process, among other issues [1]. These are just some of the risks associated with burrs. Thus, burr removal is typically necessary, which is why machined parts must be deburred before they go into service. However, the deburring process is expensive (being both time-consuming and requiring a skilled workforce). While figures are scarce, it is estimated that it can account for up to 14% and 30% of manufacturing costs in the automotive and aerospace industries, respectively [2]. This figure is largely attributed to how difficult deburring is to automate and the challenge of selecting the correct tools and operations depending on the size, location, and type of burrs present [1,3].

While literature pertaining to burr formation is sparse, there are several notable works, like that of Gillespie [4]. Gillespie established an early standard for the categorization of burrs in his study on burr formation in turning, milling, grinding, and drilling. He identified four types of burrs: roll-over burrs, Poisson burrs, tear burrs, and cutoff burrs.

* Corresponding author. Department of Mechanical and Aerospace Engineering, University of Kentucky, Lexington, KY, 40506, USA.
E-mail address: julius.schoop@uky.edu (J. Schoop).

https://doi.org/10.1016/j.ijmachtools.2023.104030
Received 31 October 2022; Received in revised form 24 April 2023; Accepted 27 April 2023
Available online 4 May 2023

The focus of this work is on roll-over burrs, which are caused by the cutting tool causing material to flow over the edge [4]. Legrand et al. [5] demonstrate how roll-over burrs tend to rotate and curl inward after numerous subsequent cuts. Roll-over burrs would nowadays typically be referred to as "exit" burrs—this terminology is attributed to their location on the workpiece.

Like other aspects of surface integrity, burr formation is heavily driven by the thermomechanical loads induced during machining, which in turn are a direct result of the selected machining parameters: feed rate, cutting speed, depth of cut, and tooling. Several works have attempted to analyze the behavior of burrs in relation to these factors [6–11]. It is widely known that cutting tool geometry and wear play a crucial role in surface integrity, yet very few works have addressed their correlation with burr formation [6]. For instance, burrs are particularly problematic in micro-machining because deburring requires higher accuracy to avoid damaging the small and delicate geometric features [7]. Aslantas et al. [8] qualitatively noted that worn end mills created larger burrs because of the increased ploughing effect; this causation was also cited by Wu et al. [9]. Furthermore, an increase in tool nose radius when turning, which is associated with greater geometric chip thinning and thus increased ploughing, has been observed to generally lead to larger burrs [10,11].

The close connection between tool-wear and burr formation is demonstrated clearly by Lee and Dornfeld [6], where they observed a substantial increase in burr height when the tool reached a catastrophic failure point (i.e., with increasing progressive tool-wear). The tool material is also important, such as in drilling of metallic glass, where a high-speed steel drill produces larger entry burrs than a tungsten carbide drill because of increased rubbing and higher wear margin [12]. It has also been shown that tool orientation and tool path have a strong influence on burr development [13–16]. For example, burr height was shown to decrease with increasing (positive) rake angle because of less shear strain in the chip [13,14]. Additionally, optimizing the tool path can significantly reduce burrs in milling operations by avoiding exits and maintaining a constant force on the tool [15,16].

Overall, published literature has clearly established that the most important cutting parameter on burr formation is the uncut chip thickness. In general, the higher the uncut chip thickness, the larger the burrs formed. In their in-situ study, Chern and Dornfeld [11] compared experimental and predicted results for exit burr height and saw that the two were in excellent agreement, showing that burr height increased proportionally with uncut chip thickness. Lee and Dornfeld [6] likewise reported a linearly increasing trend between feed per tooth (i.e., uncut chip thickness, all else being equal) and burr height. Legrand et al. [5] showed how during burr accumulation, the uncut chip thickness always had a major effect in the rise of burr height. On the contrary, varying the tool orientation and radius, as well as the workpiece exit geometry, all had a minimal effect.

Some results regarding the effect of feed rate on burr geometry have been seemingly contradictory across different workpiece materials and processes, which can be attributed to significant geometric differences and different thermomechanical loads imposed with similar feed rate parameters in various processes (e.g., milling vs turning), as well as unique material responses to these loads (e.g., brittle metallic glasses vs ductile pure metals). For instance, Bakkal et al. [12] found that a high feed rate yielded smaller burrs in the drilling of zirconium-based bulk metallic glass. However, Muhammad et al. [7] determined that the effect of feed rate was negligible in micro-milling, but Cedergren et al. [17] saw that the effect of feed rate was contingent upon grain size in turning, indicating a microstructural size effect [18]. While comparison of the effect of feed rate between different workpiece materials is difficult at best, and likely not possible in many cases, the same material (at least chemically) was used in this study. They reported that at low feed rate, burr formation was extreme for the specimen with large grains ($d \sim 127$ μm) but non-existent for the specimen with small grains ($d \sim 16$ μm). Furthermore, increasing the feed rate on the specimen with large grains heavily decreased burr formation, but the opposite was true for the small-grained specimen. This study revealed that microstructure has a major effect on burr formation, which is another aspect that has yet to be understood in the current state of the art.

Regarding the effect of cutting speed, Lee and Dornfeld [6] found that burr height decreased with increasing cutting speed at lower feed per tooth, but would increase at higher feed per tooth, which they attribute to the prolonged tool life at the lower feed rate setting. Pilný et al. [19] saw a decline in exit burr height with increasing cutting speed in the drilling of aluminum. Muhammad et al. [7] observed a major increase in burr size when increasing the cutting speed and attributed this behavior to thermal softening, which resulted in more severe plastic deformation. According to Biermann and Steiner [20], burr height generally increased as the cutting speed was increased, which was hypothesized to be the result of increased strain hardening.

In summary, burr formation is a major issue plaguing manufacturers and should be mitigated to the extent possible. Based on review of the literature, machining parameters drive the development of burr formation, which likewise implies that burr suppression may be achieved through smart process control. However, the state of research on burr formation is still primitive, as most of the pioneering work is dated and recent efforts seem to focus primarily on burr formation in micro-milling and drilling operations—there is yet to be a comprehensive study that characterizes burr formation for the more conventional, and far more widely used, machining processes of macro-milling and turning. Furthermore, most works investigate soft materials such as copper, aluminum, and steel; there is a notable shortage of studies that analyze burr formation in the exceedingly difficult-to-cut superalloys that are used to produce fatigue life-limited components for jet turbine engines, where surface integrity is imperative. Due to the presence of carbides and strengthening gamma-prime precipitates, as well as due to the high strength at elevated temperatures and limited thermal conductivity, Inconel 718 is prone to machining-induced damage and rapid tool-wear. The interactions of worn tools with this superalloy have been studied for steady-state (continuous) cutting, but the present work investigates how both sharp and progressively worn tools influence the material response at the grain/micro-scale during the complex process of burr formation.

To provide new fundamental insights into the complex burr formation process of aerospace materials, the objective of the present work was to leverage novel in-situ methods, whose potential to resolve both brittle and ductile material response at the grain-scale has yet to be fully explored in machining science, and targeted semi-analytical modeling to better understand the burr formation mechanism in dry machining of nickel-based superalloys like Inconel 718. The machining response of this popular alloy has been widely studied, and a recent review of such studies by De Bartolomeis et al. [21] points towards a future need for real-time sensing and more physics-informed modeling of Inconel 718 machining, including burr formation; the present study seeks to provide fundamental scientific insights required to formulate and calibrate such models. Notably, no prior study exploring the fundamental mechanics of burr formation at the micro-scale via high-speed in-situ microscopy methods has been performed for neither Inconel nor any other nickel alloy. The present work leverages an advanced setup capable of resolving microstructural deformation and damage evolution, as well as detailed analysis of such micrographs via digital image correlation (DIC) techniques. In this effort, the most relevant process parameters of uncut chip thickness, tool-wear, and cutting speed were considered.

2. Experimental methods

2.1. Custom in-situ testbed setup

Orthogonal cutting experiments were conducted on a custom-built in-situ testbed, shown in Fig. 1. This experimental setup consists of three independently actuated axes (x, y, and z) with a moving table that is actuated by a high-force (5000 N peak), high-velocity (252 m/min

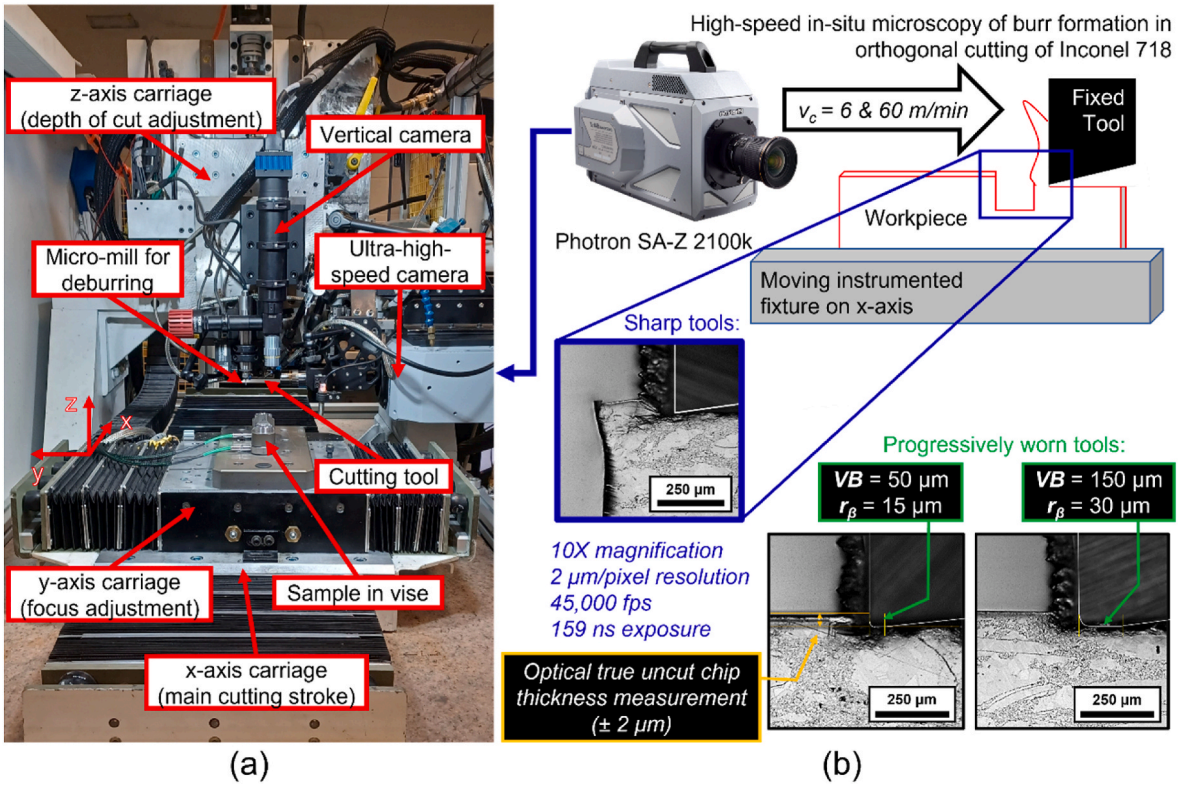

Fig. 1. (a) Overview of in-situ testbed setup and (b) schematic illustration of high-speed image acquisition in orthogonal cutting configuration.

peak) linear servo motor (type Yaskawa SGLFW-2). The table and servo motor control the main cutting stroke in the x-direction by feeding the workpiece into a fixed cutting tool at independently variable cutting speeds between zero to 252 m/min. Additional movement is allowed in the y-direction with another linear servo motor for fine focus of the tool-workpiece side engagement adjustment within ± 0.5 µm. The cutting tool is held in a custom tool holder affixed to a carriage capable of fine z-axis vertical motion for programming the desired feed (i.e., 2D uncut chip thickness). The xy-axis table holds the workpiece in a custom vise via two 0.25 inch (6.350 mm) hardened steel dowel pins (slip/interference fit with workpiece holes) and a central screw to prevent any play during cutting. Integrated within the vise are two Kistler Type 9047C piezoelectric sensors for dynamic force measurement with maximum dynamic stability (i.e., resistance to chatter during interrupted cutting).

A Photron FASTCAM SA-Z 2100k camera was used for ultra-high-speed imaging of the 2D cuts at frame rates of 45,000 per second and a resolution of 640 × 640 pixels, with each pixel resolving 2 µm via a 10X Mitutoyo M Plan microscope objective and associated video microscope unit (VMU). Primary lighting was delivered co-axially via a custom-built 5000-lumen LED light source, along with secondary external illumination (back-lighting of tool and workpiece edges and oblique/diffuse illumination of the chip) by a bifurcated light guide illuminated by a 4000-lumen white light LED light source. An additional custom vertical microscope constructed using Thorlabs components with a large field of view digital camera (type Vieworks VC-25 M) also utilizing a Mitutoyo M Plan APO 10X objective was mounted to the z-axis carriage, as shown in Fig. 1. This vertical microscope setup was used for characterizing the machined surface before and after each cutting pass.

2.2. Tool/workpiece materials and cutting parameters

All cutting tools used were Kennametal grade K68 tungsten carbide inserts. The flank face of the tools was initially ground to a 5° clearance angle, matching the alignment of the fixture of the in-situ testbed. From here, the tools were lapped/polished to either a 'sharp' or 'worn' condition using a manual grinding fixture on a series of abrasive diamond pads. To prepare the worn tools, the flank face was carefully abraded to impose the flank-wear (*VB*) in the shape of a flat facet on the bottom of the tool. This facet was incrementally ground until the desired level of artificial (perfectly uniform and geometrically defined) wear was achieved. Finally, the worn tool edges were honed on a buffing wheel charged with a diamond abrasive paste using a bench grinder to edge radii of 15 µm and 30 µm for the 50 µm and 150 µm flank-wear tools, respectively. The magnitude of the honed edge radii on the worn-condition tools was confirmed using a Zygo NewView 7300 scanning white light interferometer. Each tool was used only once, i.e., a new tool was prepared for each trial.

The Inconel 718 workpiece sample used in the experiments was in the quenched and direct aged (DA) condition with a bimodal (creep-resistant) microstructure of both 3–8 µm and 50–500 µm grain sizes distributed approximately equally throughout the sample. Grain sizes and distribution were measured using a Keyence VHX optical microscope and the mean linear intercept methodology outlined in ASTM standard E112-13 (2021). The material properties for the workpiece are shown in Table 1.

The sample material was low-stress wire-electrical discharge machined (EDM) cut from a larger forging, and subsequently milled into a rectangular geometry of approximately 50 mm × 40 mm x 6 mm. Each

Table 1
Material properties for Inconel 718-DA workpiece.

Elastic Modulus	205 GPa
Shear Yield Strength	640 MPa
Tensile Yield Strength	1100 MPa
Ultimate Tensile Strength (0.2% Offset)	1550 MPa
Poisson's Ratio	0.28
Density	8.19 g/cm^3
Hardness	46 ± 2 HRC

side was milled with a step so that the width of cut was precisely 3 mm to ensure plane strain conditions, while keeping absolute cutting forces manageable. Finally, 3 mm wide slots were milled on one side of the workpiece to form five different 'castellations', or 'edges', for a discontinuous/interrupted cutting stroke. As can be seen in Fig. 2, the width of these edges was varied to suppress harmonic vibrations that would otherwise be induced when cutting a sample with a constant step width. The length of cut, ranging from 2.5 mm to 8.6 mm, was selected to simulate the typical arc length of engagement of a single end mill tooth during a peripheral milling process. To achieve the necessary flatness and reflective finish in front of the high-speed camera for DIC analysis, the EDM-sectioned surface had to be incrementally ground and polished before being chemically etched to reveal the microstructure using a custom chemical etchant (formulated to enhance contrast for DIC). The in-situ workpiece and its microstructure are shown in Fig. 2.

Since the objective of this study was to specifically analyze the effects of uncut chip thickness, tool-wear, and cutting speed on burr formation, the sample geometry and experimental matrix (shown as Table 2) were carefully designed to consider the sensitivity and statistical significance of these factors. It was highly anticipated that uncut chip thickness would have the largest influence, which is why four different levels (ranging from 10 μm to 80 μm) were assessed. Three tool flank-wear conditions: 0 μm (i.e., 'sharp', with cutting-edge radius of approximately 5 μm), 50 μm, and 150 μm were each tested at the various uncut chip thickness values. Lastly, cutting speed was considered across one order of magnitude at settings of 6 m/min and 60 m/min—this parameter was not modified in small increments because its influence was thought to be less pronounced than that of uncut chip thickness.

It should be noted that while the nominal uncut chip thickness (h) ranged from 10 μm to 80 μm in the experimental matrix, this was only the programmed/desired uncut chip thickness. The actual/true uncut chip thickness (h_{true}) values observed in-situ (optically) byfinding the reduction in workpiece height during cutting were significantly lower depending on the cutting speed and tool-wear condition. This discrepancy is to be expected because of the minimum chip thickness (ploughing) effect, as well as machine compliance due to increasing feed forces with worn tools, which effectively push the tool out of the cut. In general, small cuts at low uncut chip thickness values tend to be less than the minimum uncut chip thickness (h_{min}), which is roughly on the order of half the value of the cutting-edge radius, causing ploughing instead of cutting [22]. The true uncut chip thickness was found by measuring the difference in pixel height between the machined and pre-machined surface on the cut videos. This difference was easily translated into microns using the conversion factor of 2 μm/pixel for the 10X objective used. By carefully measuring the true uncut chip thickness for each trial (including its variation between cuts), the measured data was effectively corrected for the effect of setup/machine compliance, which is otherwise present in any cutting experiment. Like with all the burr measurements, the uncertainty in the true uncut chip thickness was calculated by using the five edges (individual interrupted cut segments within a single cutting stroke/experiment) as the data points. The corresponding horizontal error bars to the 95% confidence interval in true uncut chip thickness were incorporated into all burr profiles.

Table 2
Experimental matrix.

Cutting Speed (v_c) [m/min]	Flank-Wear (VB) [μm]	Uncut Chip Thickness (h) [μm]
6	0	10
	50	20
60		40
	150	80

2.3. Analyzing burrs with optical microscopy and DIC

Burr data was quantified via two methods: (i) optical microscopy for measuring burr geometry and (ii) DIC for calculating the displacement (and subsequently the normalized stress), at the burr root, which will be explained in greater detail later. Following each cutting trial, the burrs were 3D-scanned on a Keyence VHX-7000 digital microscope by photographing each individual edge using the microscope's 3D image-stitching (focus-stacking) feature. Subsequent analysis was conducted using the VHX-7000 measurement software.

Open-source software, Ncorr [23], was used to perform the DIC analysis on individual high-speed in-situ image frames in MATLAB. For this procedure, 'reference' images were obtained by recording the workpiece passing in front of the camera in the unloaded (pre-cut) condition. Then, 'current' images were obtained by recording the workpiece during the cut itself. For a given machining condition, the horizontal (u) and vertical (v) subsurface displacement fields were calculated in Ncorr. The practical resolution of these displacement fields was found to be on the order of 50 nm, i.e., about two orders of magnitude greater than the 2 μm/pixel optical resolution of the experimental setup (roughly 1/50th micropixel resolution). This level of performance is consistent with the well-established limits of performance of the DIC technique, which routinely achieves 1/100 micropixel resolution.

3. Characterization of burr development

According to Gillespie [4], burr formation occurs because of three possible mechanisms: bending of the chip, lateral extrusion of material,

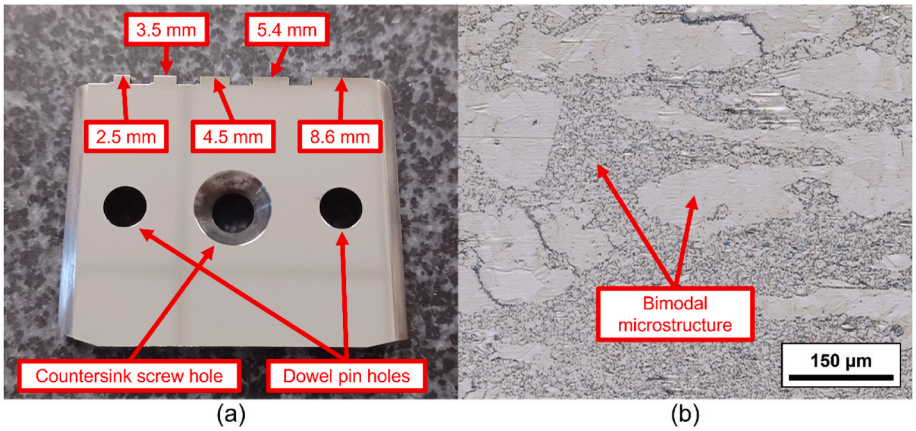

Fig. 2. Images of (a) geometry and (b) microstructure of polished and slotted in-situ Inconel 718 workpiece sample. Slots were variably spaced to suppress chatter. The bimodal microstructure of the DA Inconel workpiece material is tailored for creep-resistant turbine applications.

and tearing of the chip from the workpiece—each of these leads to different types of burrs. The focus of this study is on the first and second mechanisms. Exit burrs are caused by material bending over the edge due to lower energy being required than shearing [4,24]. Tearing of the chip is prevalent at high uncut chip thickness, where the large shear strain from the chip bending over an edge or corner fractures off material from the workpiece. This results in negative exit burrs, to be discussed in greater detail later.

Ko and Dornfeld [13] expanded upon the exit burr criteria set forth by Gillespie by establishing three stages for exit burr formation: (i) burr initiation, (ii) burr development, and (iii) final burr formation. These three stages are shown during a cutting stroke in Fig. 3: Fig. 3a and b are frames during the cut itself, and Fig. 3c is captured after the cut with the tool passing over the workpiece where there is no contact. The slow-motion footage of this experiment can also be viewed as Video 1 in the supplementary materials.

Supplementary video related to this article can be found at https://doi.org/10.1016/j.ijmachtools.2023.104030

Fig. 4 illustrates the stages of exit burr formation during the initiation and development stages using DIC displacement fields: Fig. 4a–d are during initiation and 4e-h are during development. Fig. 5 is a schematic representation of the various metrics used to quantify exit burrs, where this schematic is at the onset of burr formation. Exit burrs occur when steady-state chip formation transitions into burr formation, and is indicated by the appearance of a so-called negative shear plane [13,25,26], as shown in Figs. 4 and 5. The onset of the negative shear plane is given by the initial negative shear angle (β_0), as shown in Fig. 4c,g and 5. The negative shear plane and angle pivot about a plastic hinge [11,13], also known as the "exit burr root", which is illustrated by Point B in Fig. 5—this hinge was also identified by Gillespie [4]. As can be observed in Fig. 4b and c, the burr root is displaced prior to burr development, as the most intense elastic deformation concentrates around the edge of the workpiece. Lastly, it can be seen from Fig. 4d that at exit burr initiation, plastic shear is localized around the tool tip, which is the primary deformation zone (PDZ) of chip formation.

At the onset of burr formation, shown in Fig. 4c, a negative shear zone forms and subsequent deformation is localized along this plane for sharp tools. The plastic zone during burr formation with worn tools was significantly larger, as will be shown in Section 3.2. As a result, the interactions between microstructure and the burr formation process differ substantially between sharp and worn tools, while the overall stages of burr formation from initiation to shear localization are qualitatively consistent across various process parameter conditions. Notably, the high degree of strain localization when cutting with sharp tools was observed to result in so-called negative (fractured) burrs, to be discussed in Section 5.

Once exit burr formation is complete, they can be classified as either "positive" (where the burr extrudes outward from the edge of the workpiece) or "negative" (where the burr is sheared off or fractures and carried away with the chip), leaving the appearance of a 'shoe' or the letter 'L' on the chip. Anecdotally, along with significant tool-chip adhesion in cutting of nickel-based superalloys, negative burrs have been observed by the authors to coincide at times with catastrophic tool edge fracture, which is likely due to a combination of high strain rate (shock loading) and the reversal of compressive cutting loads into a tensile inertial acceleration load imposed by the fractured chip. However, this phenomenon requires further investigation and is therefore not addressed in the present work. The negative burr phenomenon itself will however be discussed in greater detail in Section 5. Schäfer [27] was the first to introduce various parameters for measuring positive exit burrs, which were refined by Ko and Dornfeld [13]. These parameters were foundational in establishing the convention for measuring exit burr geometry and the same framework is used in this study. Shown in Figs. 5 and 6 are annotated schematics that label the many different metrics used for measuring exit burrs.

As can be seen in Fig. 6, there are many different variables for characterizing a positive exit burr. The most noteworthy of these is the burr thickness (b_t), which is the distance from the top of the machined surface to the burr root (i.e., the plastic hinge from before). Besides the thickness, there is the burr height (b_h), which is how much the burr extrudes outward from the edge of the workpiece. The thickness and height are the most important parameters because they are not only most indicative of the overall size, but they indicate the degree of difficulty for burr removal [28]. The inclination angle (ψ) shows how acute or obtuse the burr is.

A notable observation of the present study was an additional angle not previously identified by other researchers. A proposed name for this new angle is the *initiation angle* (η). As shown in Fig. 6f, this angle is indicated by a very shallow slope as the machined surface begins to point downward. Other works, like that by Ko and Dornfeld [13], assumed the top of the workpiece to be flat after the cut is complete—this would entail measuring to the theoretical top of the workpiece where there is no material, which is not representative of the true burr thickness. Furthermore, several other variables can be measured with respect to this location because it appears to represent the burr initiation point. This shallow angle is being assumed as the onset of burr initiation because it is the only indicator of the transition from steady-state chip formation with large associated process forces to burr

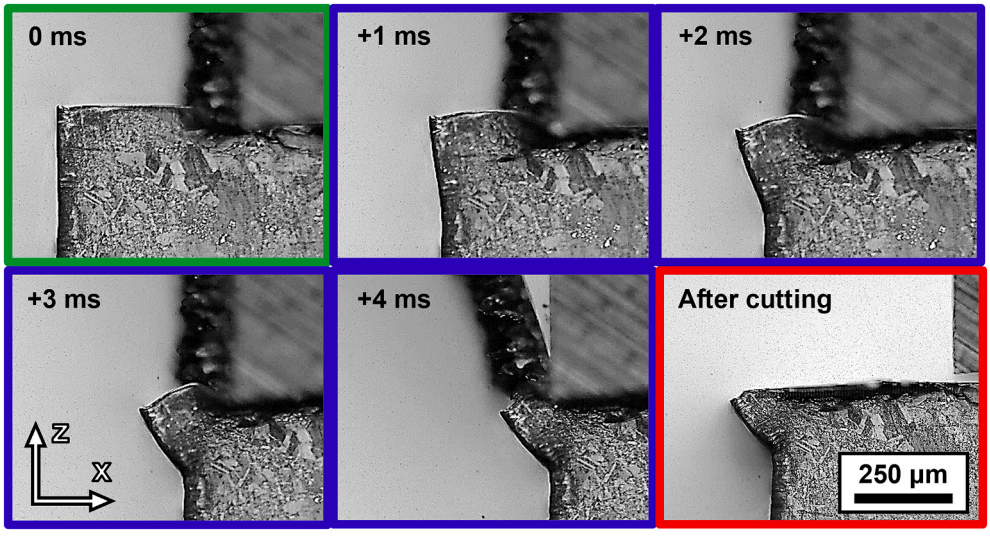

Fig. 3. Representative sequence of high-speed in-situ micrographs illustrating exit burr initiation (green), development (blue), and final formation after cut (red). Similar micrographs were analyzed to study interaction of microstructure and process parameters on ductile and brittle material deformation modes during burr formation. $VB = 0$ µm, $h = 80$ µm, $v_c = 6$ m/min. (For interpretation of the references to color in this figure legend, the reader is referred to the Web version of this article.)

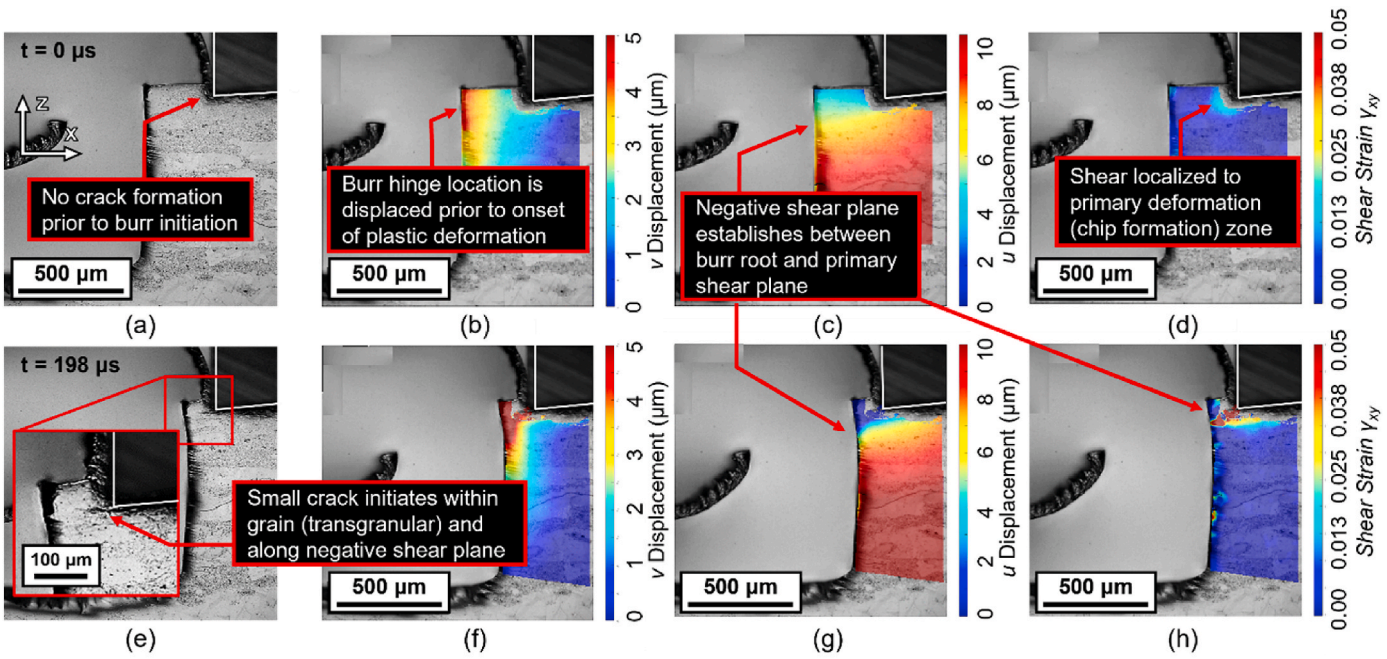

Fig. 4. (a, e) In-situ optical micrographs and corresponding DIC analysis of (b, c, f, g) displacements and (d, h) shear strains during the most common 'positive' burr formation at (a–d) initiation and (e–h) development. DIC analysis revealed substantial displacement and strain localization during burr development, including localized cracking, highlighted with the inset in (e). $VB = 0$, $v_c = 60$ m/min, $h_{true} = 30$ µm.

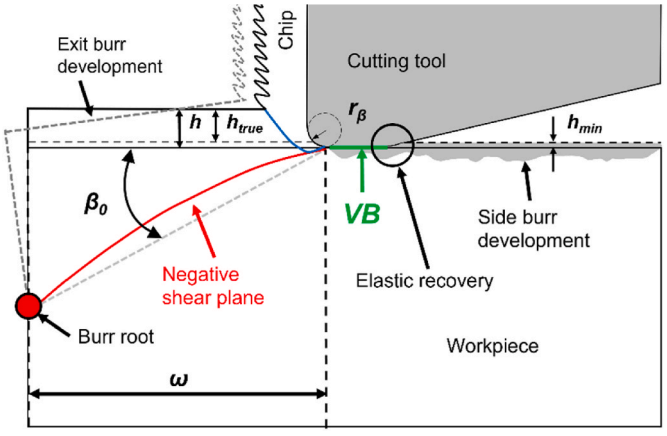

Fig. 5. Schematic of exit burr initiation and associated burr metrics. Based on these metrics, subsequent in-situ and post-machining analysis of burrs was carried out to study the effects of process parameters and tool-condition on burr development.

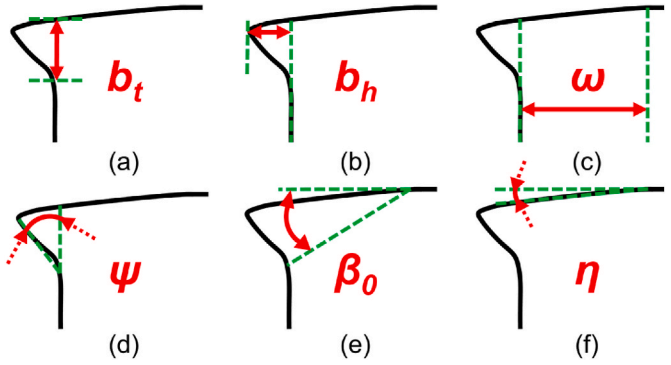

Fig. 6. Schematic representation of exit burr parameters: (a) thickness (b_t); (b) height (b_h); (c) initiation distance (ω); (d) inclination angle (ψ); (e) initial negative shear angle (β_0); (f) initiation angle (η).

formation and the associated change (reduction and re-alignment) of said forces. The burr initiation point is more easily observed when viewing the workpiece from above (see Fig. 7). From this, the initial negative shear angle can be measured using the burr root (i.e., bottom of the burr thickness) and the horizontal, theoretical top of the workpiece. Moreover, the exit burr initiation distance (ω) can be measured by simply taking the distance between the burr initiation point and the edge of the workpiece.

Since the sample workpiece featured five interruptions/edges, there were five potential exit burrs corresponding to each trial, which allowed for five data points to be measured for each parameter. To accurately represent the inherent statistical variation of each of the burr parameters under investigation, a 95% confidence interval based on the Student's t-distribution was used to eliminate outliers beyond the upper and lower control limits. Finally, regression fits were implemented to illustrate statistically significant trends and deviations between the different wear conditions. In cases where there was no statistically significant difference between wear conditions, a single, combined (average) regression was calculated to highlight the overall trend.

3.1. Exit burr profiles

This section will discuss numerous parameters pertaining to exit burr formation, including both a measurement of the final burr geometry, and various distances and angles and distances at the onset of development (i.e., initiation).

3.1.1. Final exit burr geometry

Figs. 8 and 9 show the profiles for the average exit burr thickness (b_t) and exit burr height (b_h). As stated previously, the results plotted are the geometric means across the five edges after outliers beyond the confidence interval were eliminated. Notably, all burr parameters were significantly (i.e., within a 95% confidence interval) influenced by the uncut chip thickness. However, as can be observed, tool-wear does not have a statistically significant influence on burr size in most cases except

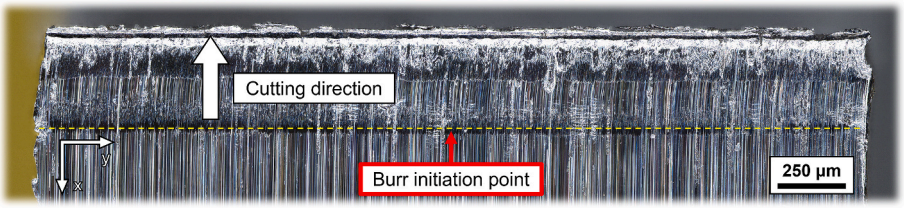

Fig. 7. Visual of burr initiation point from a vertical view of the machined surface. The initiation point marks the transition from steady-state chip formation to the beginning of burr formation due to the development of the subsurface negative shear plane. This transition can be directly observed in plane view of the machined surface due to the slightly negative initiation angle η.

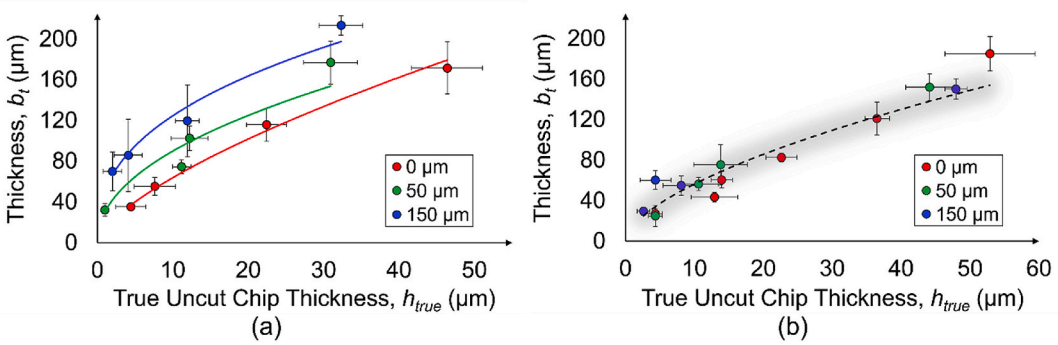

Fig. 8. Average profiles for exit burr thickness (b_t) at (a) $v_c = 6$ m/min and (b) $v_c = 60$ m/min for the three tool-wear conditions. Results are consistent with the previously reported increase in b_t with uncut chip thickness. Tool-wear had a statistically significant effect at the low cutting speed but did not exhibit a significant effect at the high cutting speed.

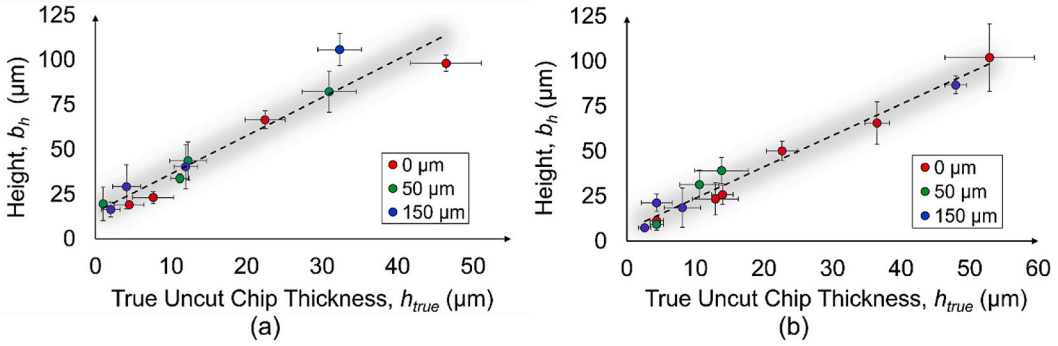

Fig. 9. Average profiles for exit burr height (b_h) at (a) $v_c = 6$ m/min and (b) $v_c = 60$ m/min for the three tool-wear conditions. No statistically significant effect of tool-wear was observed and b_h increased proportionally with uncut chip thickness at both cutting speeds.

for the condition of b_t at low cutting speed (Fig. 8a). It is hypothesized that this is attributed to the significant amount of cold work and strain hardening of progressively worn tools at low cutting speeds. While thermal softening at increased cutting speed may counteract strain hardening to some degree (affecting the plastic response of the workpiece material in the subsurface ahead of the tool), the lack of thermal softening at lower speeds would magnify the effect of tool-wear on b_t, as well as the initiation distance (ω). Indeed, tool-wear did exhibit a significant effect on ω, as can be seen in Fig. 11. The apparent connection between b_t and ω may be explained by the increasing stress distribution in the subsurface that is known to be associated with increasingly worn tools [29].

Furthermore, deeper subsurface deformation at the exit would mean that the exit burr root would be pushed down lower. No other researcher has investigated exit burr development with respect to flank-wear, but it has been shown that b_h increases with higher tool nose radius, which is known to be a factor that favors increased ploughing and material side-flow [10,30,31]. Furthermore, Lee and Dornfeld [6] saw that tool-wear only caused a significant increase in b_h when there was catastrophic failure. Otherwise, they saw only a gradual but minor increase as tool-wear progressed. No significant trend could be seen for the inclination angle (ψ). The only other work to consider ψ is Ko and Dornfeld [13], who demonstrate how ψ changes at different distances from the edge of the workpiece, yet they likewise did not report significant effects of cutting parameters on this value.

3.1.2. *Cutting speed analysis*

To further investigate the observed relationships between cutting speed and burr geometry, as well as the effect of tool-wear, analysis of cutting force data obtained during the in-situ trials was carried out. Since the raw data points were too numerous, power law regressions were calculated for each set of cutting and feed forces, respectively, at each speed and tool-wear condition. The results of this analysis are shown in Fig. 10. As can be seen, the lower cutting speed of 6 m/min resulted in a higher force for each tool-wear and uncut chip thickness condition. Moreover, increasing tool-wear resulted in significantly larger forces, with the feed force increasing most notably. Interestingly, the relative difference between the three tool-wear conditions was more

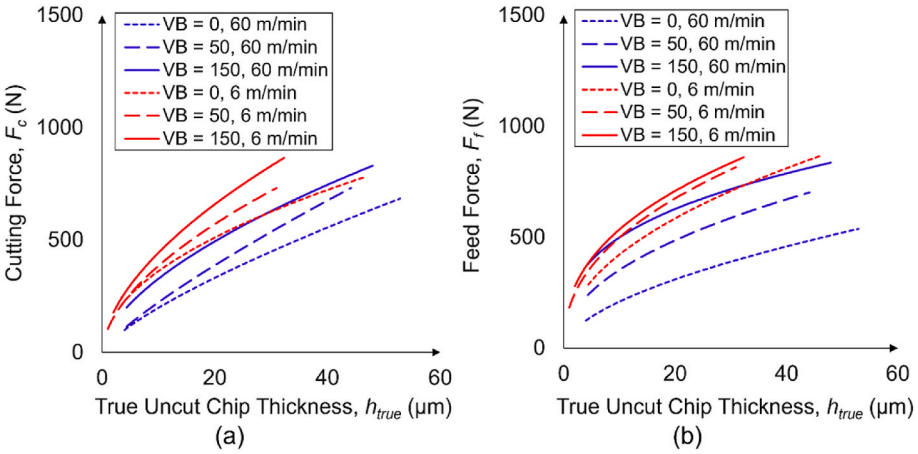

Fig. 10. Inconel 718 orthogonal (a) cutting force and (b) feed force power law regression fits for $v_c = 6$ m/min (red) and $v_c = 60$ m/min (blue). Higher tool-wear and a lower cutting speed resulted in larger forces, with the feed force exhibiting greater sensitivity to tool-wear due to the ploughing effect. (For interpretation of the references to color in this figure legend, the reader is referred to the Web version of this article.)

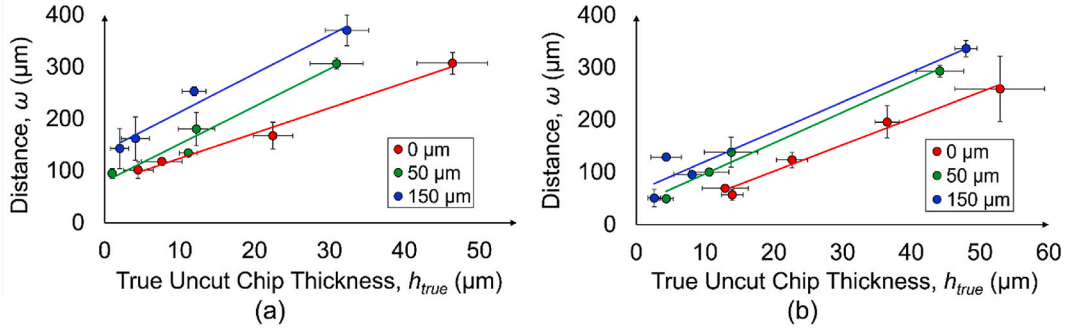

Fig. 11. Average profiles for exit burr initiation distance (ω) at (a) $v_c = 6$ m/min and (b) $v_c = 60$ m/min. Results showed a significant effect of tool-wear at both cutting speeds due to the extent of subsurface plastic and elastic deformation induced by worn tools.

pronounced at the higher cutting speed of 60 m/min, as shown in Fig. 10b. This observation, along with the general trend for forces to increase with decreasing speed and increasing wear generally, is interpreted as evidence of increasing mechanical loading at lower speeds and greater tool-wear. At the higher cutting speed, both strain rate hardening, and thermal softening are at play, so the behavior of the feed force, which is closely tied to the ploughing effect, is more complex. Overall, the values of cutting and feed force were roughly comparable due to the significant ploughing and strain hardening encountered when cutting of Inconel 718.

3.1.3. Exit burr initiation

Figs. 11 and 13 show the average profiles for the exit burr initiation distance (ω) and initial negative shear angle (β_0). From Fig. 11, as expected, ω increased with uncut chip thickness—this outcome was also found by Régnier et al. [32] in their in-situ study. Moreover, for both cutting speeds under investigation, ω also increased with tool-wear. Notably, ω was on average 36% higher at the low cutting speed —this result is echoed by Ko and Dornfeld [13]. This observation is consistent with the hypothesis that lower cutting speeds result in increased strain hardening, which would necessarily increase the lateral dimension of plastic deformation around the tool-workpiece contact area, like the effect of tool-wear discussed previously. Further, unlike previous studies [13,32] that addressed ω, the present work also encompassed the important effect of tool-wear. Greater analysis of in-situ micrographs and associated DIC analysis was conducted to elucidate the mechanisms that give rise to the observed influence of wear on burr initiation distance, as well as burr thickness at low cutting speeds.

It is hypothesized that ω increases with tool-wear because of a rise in the size of the mechanical stress field within the workpiece's subsurface ahead of the tool. Since the tool-workpiece contact area increases with tool-wear, the lateral dimension of the zone with sufficient stress to cause plastic deformation (i.e., greater than the flow stress of the workpiece material) is likewise increased. Based on this hypothesis, a more detailed analysis using the steady-state displacement fields was undertaken via DIC software, and the results are shown in Fig. 12.

As can be seen in Fig. 12, worn tools impose very different subsurface thermomechanical loads—the height and width of the stress field increased considerably with tool-wear. While the morphology of the displacement fields is approximately constant with wear, the overall size (which reasonably approximates the state of stress in the workpiece subsurface), increases with tool-wear. As the color scale of Fig. 12 was held constant for the horizontal (u) and vertical (v) displacements, respectively, the relative extent of the yellow displacement contour (1.3 μm relative u-displacement and 1.1 μm relative v-displacement) may be taken as a quantitative indication of the scale of the stress field for each tool-wear condition.

From Fig. 13, β_0 was not significantly affected by tool-wear condition, but varied slightly with uncut chip thickness, generally increasing to a steady-state value between 30° and 35°. Previous work had likewise shown that β_0 for exit burr fracture to be mostly independent of cutting conditions, particularly at larger feed (uncut chip thickness) values [32, 33]. The observed consistency of the β_0 with respect to cutting parameters suggests that it behaves in a manner analogous to the primary shear angle. Notably, the shear angle is well-known to be strongly affected by the tool rake angle, which has been shown to strongly

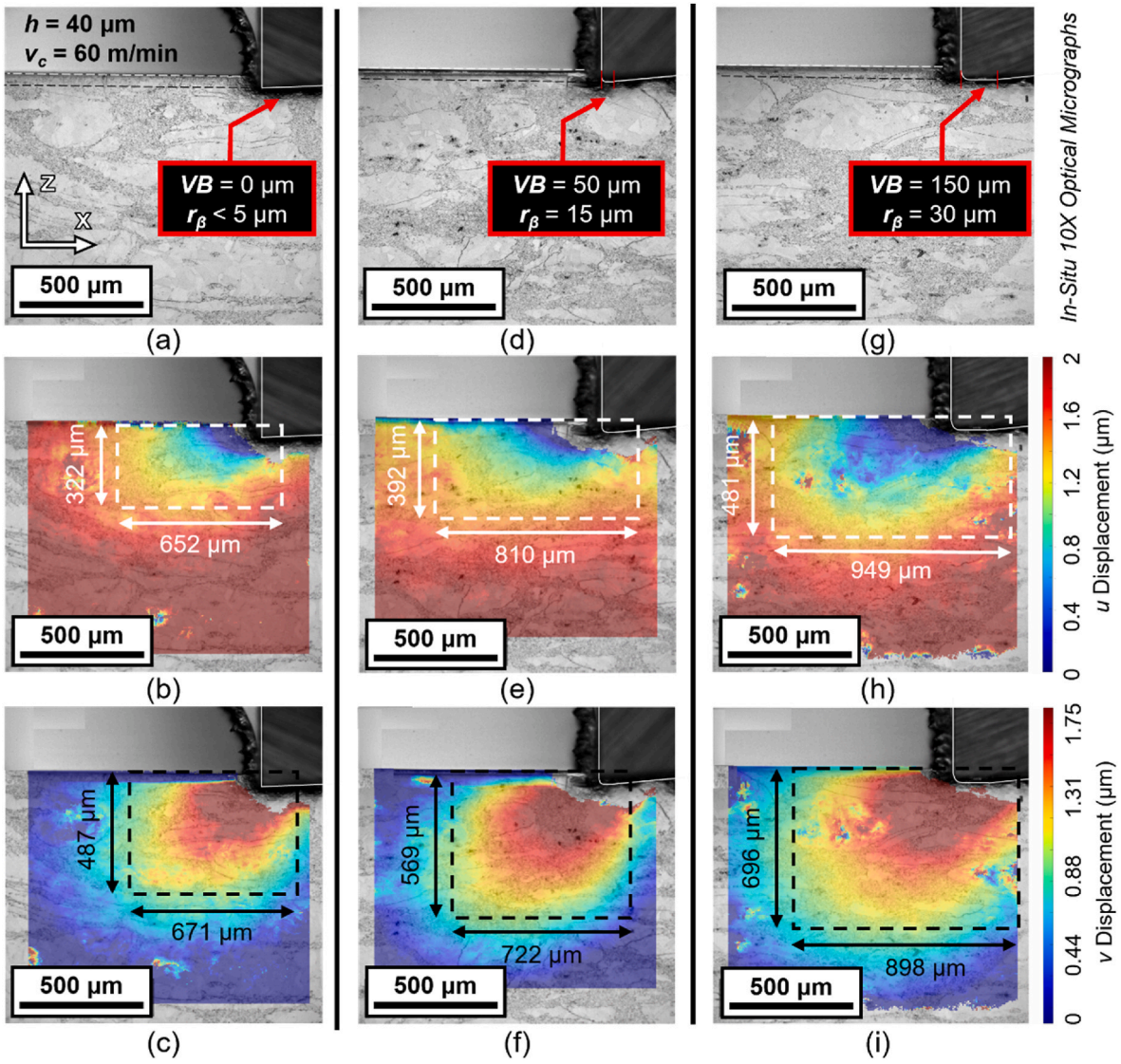

Fig. 12. Optical micrographs (10X magnification, 159 ns exposure) and subsurface DIC analyzed displacement fields for (a–c) $VB = 0$; (d–f) $VB = 50$ µm; (g–i) $VB = 150$ µm at $v_c = 60$ m/min and $h = 40$ µm. Each successive hue in the DIC plots corresponds to approximately 200 nm of differential displacement, clearly illustrating the increasing extent of subsurface elastic deformation with progressively worn tools.

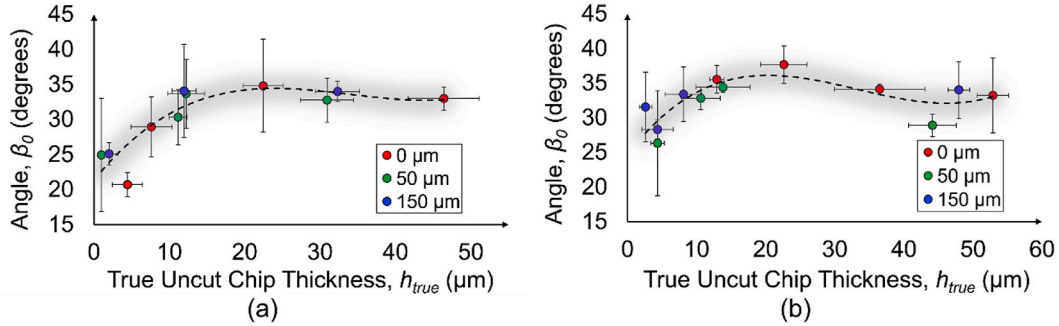

Fig. 13. Average profiles for initial negative shear angle (β_0) at (a) $v_c = 6$ m/min and (b) $v_c = 60$ m/min. No significant effect of tool-wear was observed, and β_0 followed a similar qualitative trend as would be expected for the primary shear plane with increasing uncut chip thickness, suggesting that similar physical mechanisms and size effects influence both chip formation and burr formation.

influence the initiation distance (ω) [32], so an investigation of the correlation between rake angle and β_0 will need to be undertaken in future work. No significant difference between any of the cutting conditions was observed for the newly identified initiation angle (η). The angle was always very shallow, typically always varying from 2° to 5°.

The cutting speed, which did not exhibit consistent effects on exit burr formation in studies by other authors, was found to have a significant effect on certain burr parameters and a negligible effect on others

in the present work. One such parameter that was affected heavily by cutting speed is the exit burr thickness (b_t)—on average, it was 30% higher at the low speed than the high speed. While the change in b_t with tool-wear was insignificant at high speed, the worn tools produced considerably higher b_t at low cutting speed. This observation suggests that when cutting with worn tools at lower speeds, deeper subsurface alterations are generated since the hinge point must be lower for the thickness to increase. This is plausible considering that cutting tools have much more difficulty cutting at low speeds due to increased strain hardening and reduced thermal softening of the workpiece material, leading to increased cutting forces and mechanical loads in the workpiece subsurface. Another parameter that appeared to be influenced by cutting speed is the initiation distance (ω), which was noticeably higher at the low cutting speed, likely due to increased stress intensity under such 'cold' conditions when compared to the higher cutting speed.

Parameters that were observed to be independent of cutting speed include the exit burr height (b_h), which was basically identical considering uncertainty. Other works that analyzed b_h are mixed: Pilný et al. [19] saw that b_h decreased with increasing cutting speed whereas Lee and Dornfeld [6] saw that it only decreased with increasing cutting speed at low uncut chip thickness, after which it began increasing with cutting speed—this was also observed by Nakayama and Arai [14]. Therefore, b_h can be largely independent of cutting speed and tool condition, yet it does increase along with the uncut chip thickness. Moreover, the inclination angle (ψ), initial negative shear angle (β_0), and initiation angle (η) were all considered to be constant across cutting speeds.

3.2. Tool-wear comparison of subsurface deformation

As was exhibited in Section 3.1, tool-wear had a significant correlation with some burr parameters. Referring to Fig. 11, tool-wear greatly altered the behavior of the exit burr initiation because of a much larger mechanical stress field, i.e., both plastic and elastic deformation, ahead of the tool. To further elucidate the effect of tool-wear on the burr formation process, further analysis of in-situ micrographs was conducted utilizing DIC.

To better understand the effect of tool-wear on subsurface deformation, a series of DIC plots were generated at the low cutting speed to supplement the plots at high speed previously shown in Fig. 12 at the

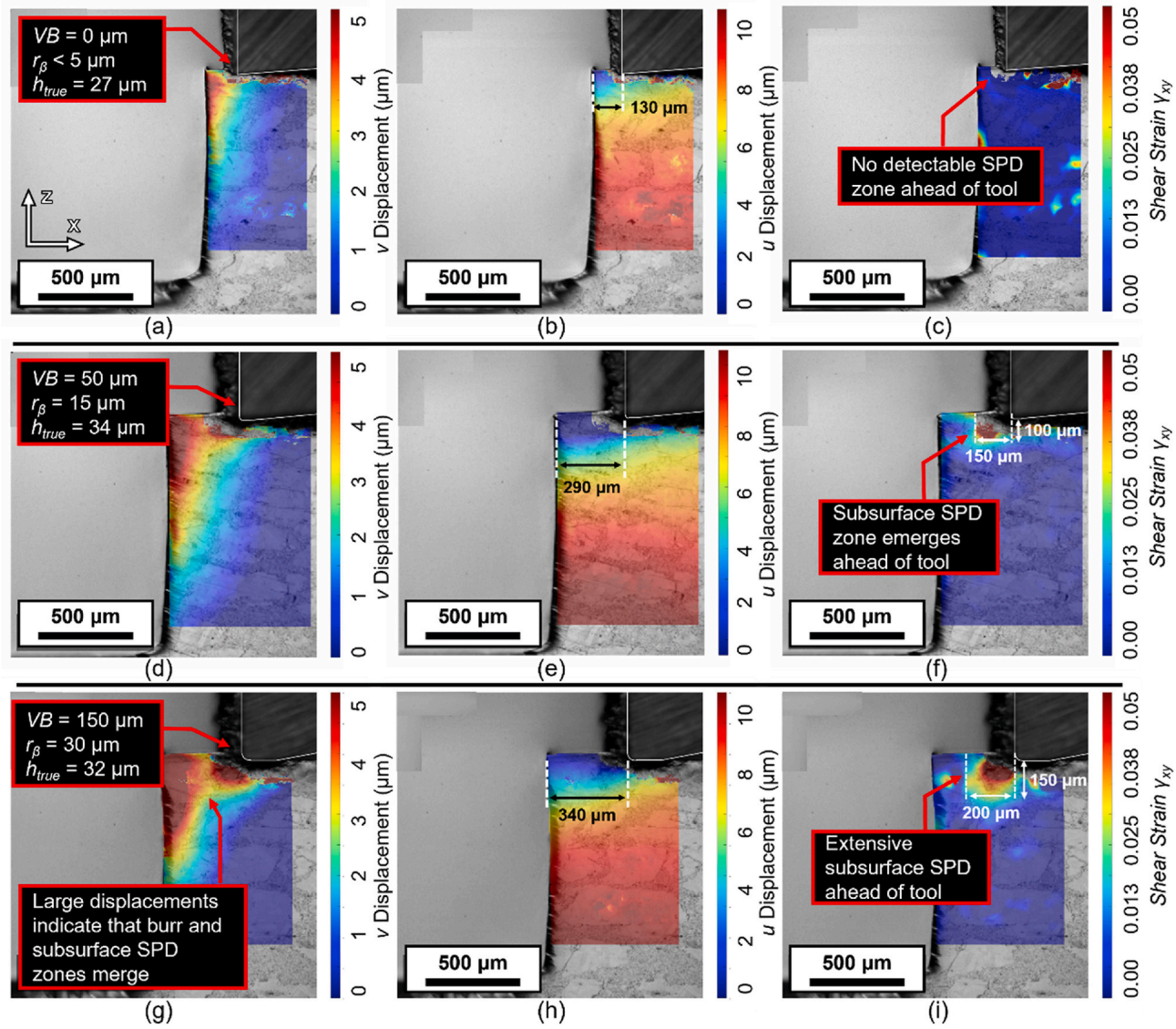

Fig. 14. Subsurface full-field DIC analysis illustrating the state of (a, b, d, e, g, h) displacement and (c, f, i) shear strain at the instance of burr initiation for (a–c) $VB = 0$; (d–f) $VB = 50$ µm; (g–i) $VB = 150$ µm at $v_c = 6$ m/min. Tool-wear had a substantial effect on both displacements and strain, resulting in the observed increase in initiation distance with tool-wear at similar true uncut chip thickness.

burr initiation stage. Moreover, as the burr height was found to depend most strongly on tool-wear at low cutting speeds, analysis of such a low-speed condition was considered particularly relevant. The relevant plots are shown below in Fig. 14. As can be seen, the severity of displacement along the workpiece edge is significantly larger for the worn tools. Similarly, the exit burr initiation distance rose accordingly as tool-wear increased—this same effect was also observed at high cutting speed in Fig. 12.

As previously stated in Section 3, at the onset of burr initiation, plastic shear remains localized within the PDZ. From Fig. 14c,f,i, the size of the PDZ, or SPD (severe plastic deformation) zone, is notable for $VB =$ 50 μm and $VB = 150$ μm, but could not be resolved for the sharp tool, showing that no meaningful subsurface SPD zone was present when cutting with unworn tools. This further emphasizes the notion that worn tools induce higher mechanical loads on the subsurface, including an increasingly larger SPD zone as well as a larger elastic stress field, as previously illustrated in Fig. 12 for steady-state (uninterrupted) cutting.

While DIC analysis clearly reveals the influence of tool-wear on the elastic and plastic deformation of the workpiece during both steady-state cutting and the burr formation process, further analysis on the effect of microstructure and process-induced defects (cracks, folds, tears, etc.) is required to understand the way process parameters and tool condition influence burr formation. To this end, Fig. 19 shows the optical micrographs corresponding to the DIC fields in Fig. 14 but at all three stages of exit burr formation. From these figures, it can be seen how the SPD profile, indicated by a dashed yellow line, is much more pronounced with increasing levels of tool-wear.

To summarize, results were consistent with those of prior studies, showing that the most crucial machining parameter is the uncut chip thickness, which significantly increased burr size (thickness and height), as was the conclusion of many researchers [7,11,13,14,30]. Analysis of burr parameters showed that most burr metrics were found to not be significantly affected by tool-wear and cutting speed. However, tool-wear and cutting speed influenced some metrics under certain conditions. For example, exit burr thickness increased greatly with tool-wear at low cutting speed. Cutting speed was demonstrated to have a clear influence on burr thickness and initiation distance. Other metrics, such as inclination angle, initial negative shear angle, and initiation angle remained constant across all cutting conditions. Further, while tool-wear was found not to have a significant influence on several final burr geometry metrics, high-speed micrographs and associated DIC analysis showed that wear strongly affects subsurface deformation by inducing a larger stress field ahead of and underneath the tool. This effect explains the higher initiation distance and burr height observed for worn tools, particularly at low cutting speed, which exhibit lower thermal softening effects and thus reveal mechanical effects more clearly than higher speeds. Moreover, a substantially larger subsurface SPD layer observed with worn tools was found to first initiate and then quickly suppress crack growth, leaving a series of plastically compressed cracks within the machined surface. Further work will be required to study the influence of these compressed cracks on ductility and fatigue strength of Inconel 718 components machined with progressively worn tools.

4. DIC displacement and stress at the burr root

In past modeling efforts for burr formation, the negative shear plane in Fig. 5 was assumed to be straight [4,11,13,14,34]. In reality, it is convex with an approximate radius, R, and it has been well-understood that negative burr fracture occurs along this shear plane (also referred to as a 'slip-line') [26,33,35,36]. Experimental results of the present work have indeed confirmed this to be the case, as for all cases where negative burr formation was observed, the fractured surface had a very defined curvature (see Figs. 17 and 20).

Furthermore, there is reason to believe that the curvature of the negative shear plane coincides with the contours of the vertical displacement field, and similarly, the flow stress field. Using non-contact strain measurement via DIC, the displacement field for all experimental trials was obtained. Rather than compute the large plastic strains and rigid body displacements that occur during burr formation, an alternative approach of analyzing the steady-state displacement field was pursued to better understand the subsurface state of stress. As displacements are proportional to stress only within the elastic limit, careful interpretation of DIC-analyzed displacement fields during cutting is required, as in reality both elastic and plastic strains will be present during cutting.

4.1. DIC displacement at the exit burr root

To date, the only other work that had used in-situ DIC to characterize burr formation is by Régnier et al. [32]. They used DIC to identify the appearance of the initial negative shear plane by observing a region of intense compression at the exit burr corner when analyzing displacement in the horizontal direction. Using the initial negative shear angle (β_0), the initiation distance and exit burr thickness (b_t) were determined. However, they did not observe β_0, but instead one of the varying negative shear angles (β), which is after burr initiation has already started.

Thus, this study aimed to further the DIC analysis performed by Régnier et al. [32] by finding the true displacement at the burr root using the steady-state vertical displacement field. This was made possible since the burr initiation distance and the burr thickness were already measured empirically, so the approximate coordinate of the burr root on the displacement field could be found by measuring relative to the cutting tool tip. An overview of the DIC-measured displacement values at the burr root is shown Fig. 15a, while Fig. 15b summarizes the model-analyzed normalized stress at this location. As can be seen, the average vertical displacement at the hinge point was 1.45 μm, with a

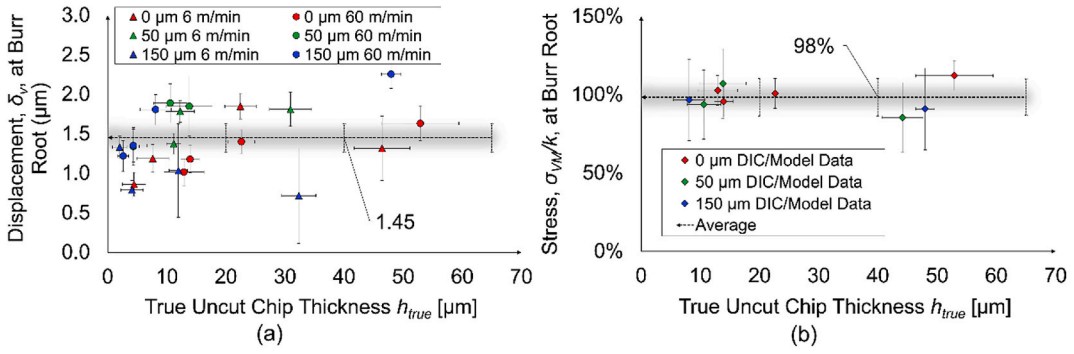

Fig. 15. Summary of (a) v-displacement DIC data and (b) model-analyzed normalized stress at burr root. These results indicate that regardless of speed and tool-wear condition, the state of normalized stress at the burr root is approximately equal to the room-temperature shear flow stress of the DA Inconel 718 workpiece material.

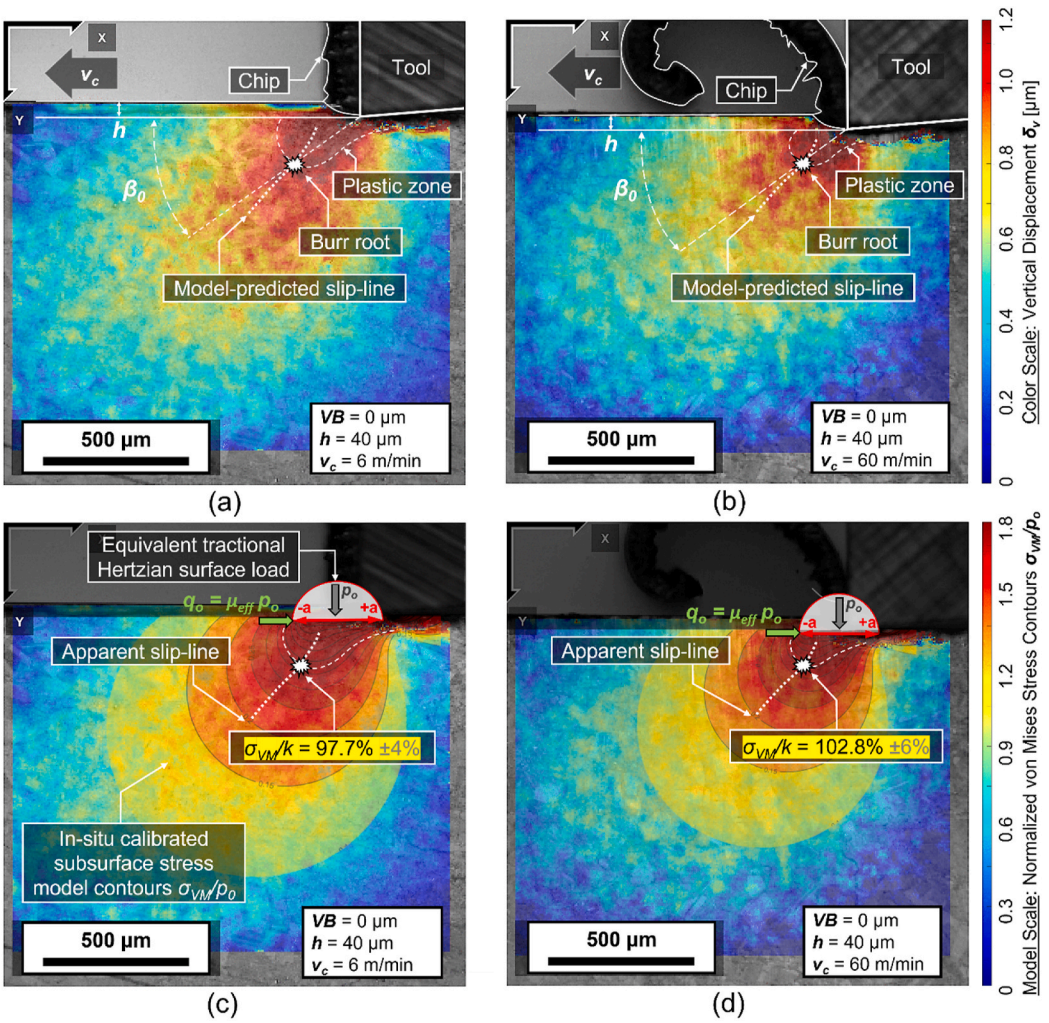

Fig. 16. Vertical displacement fields from DIC analysis overlaid on in-situ optical micrographs for (a) $v_c = 6$ m/min and (b) $v_c = 60$ m/min. Model-generated von Mises (σ_{VM}) stress fields were overlaid on vertical displacement fields for (c) $v_c = 6$ m/min and (d) $v_c = 60$ m/min to illustrate the process in which the subsurface stress model was calibrated for quantitative conversion of measured displacements into model-predicted stress. Notably, the extent of the displacement and stress fields far exceeds the near-surface plastic zone.

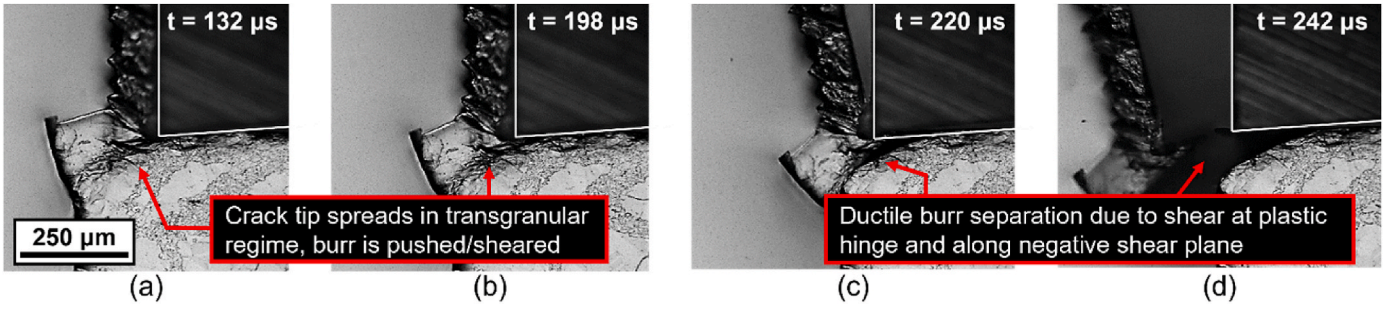

Fig. 17. Process of fracture in negative exit burr formation ($VB = 0$ µm, $v_c = 60$ m/min, $h = 80$ µm). In-situ micrographs show clear evidence of non-uniform crack propagation due to complex interactions with the bimodal microstructure of the workpiece material.

95% confidence interval of ± 0.18 µm for the sample set of the 24 measurements that were taken. It should be noted that there is no direct relationship between displacement and stress or strain since the relationship between these may well be within the plastic regime and thus exhibit highly non-linear constitutive behavior that requires knowledge of strain, strain rate, and temperature. Nevertheless, the existence of a reasonably consistent average displacement value appears to suggest some similarity in the state of stress and strain at the burr hinge point. Based on this insight, further analysis of the state of stress using a semi-analytical modeling approach was conducted.

4.2. Semi-analytical analysis of burr initiation mechanics

As discussed previously, linearly proportional conversion between displacement and stress is only possible within the elastic limit, and thus a semi-analytical approach was adopted to determine the relationship

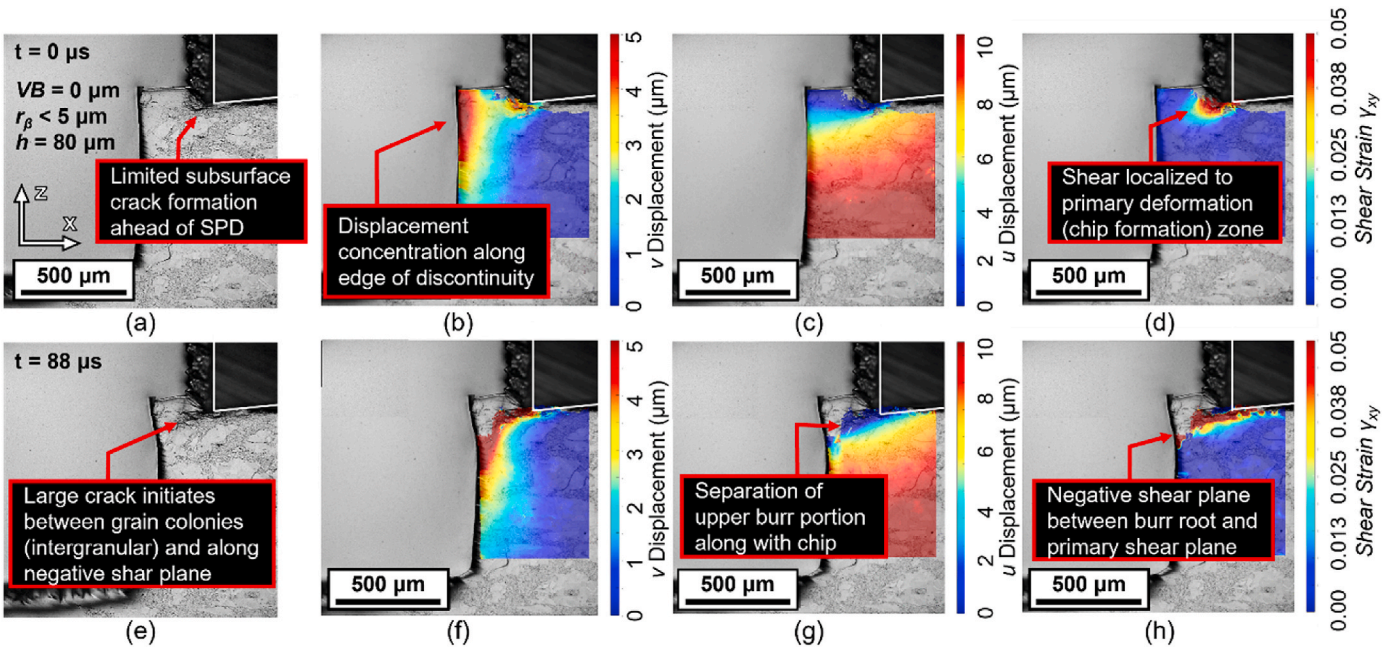

Fig. 18. (a, e) Optical micrographs and full-field DIC analysis of (b, c, f, g) displacements and (d, h) shear strain behavior during negative burr formation at (a–d) initiation and (e–h) development. Image sequence corresponds to same in-situ cutting trial shown in Fig. 17. Results show that negative burr formation is initiated by large intergranular cracks preceding ahead of cutting tool in an intergranular fracture mode.

between displacement and stress at the burr root. This approach was previously developed by Platt et al. [37] to study and predict residual stress formation due to the thermomechanical loads imposed during cutting. In the present study, a similar methodology was adopted. Specifically, the DIC data of the vertical displacements (δ_v) was used to calibrate an analytical model of subsurface stress. The primary factors of this model are the effective half-width of contact (a) and the normalized equivalent normal pressure (p_o/k) where p_o is the peak contact pressure and k the flow stress of the workpiece material. Both variables can be directly calibrated based on in-situ displacement field and cutting force data, as described in Schoop et al. [38]. The model being used is a modified tractional Hertzian contact model, first developed and employed by Johnson and co-workers [39,40] and widely used to predict contact mechanics and stresses in sliding, burnishing, and cutting processes since.

As can be seen in Fig. 15b, the effective normalized stress at the hinge point was determined to be 98% of the workpiece material flow stress, with a 95% confidence interval of ± 12% due to the limited number of total available samples (9 DIC plots of sufficient quality for various tool-wear and uncut chip thickness values were analyzed). In other words, it appears that burr initiation occurs when the outermost stress contour ahead of the cutting tool, which is equal to the flow stress of the workpiece material, intersects the vertical edge of the workpiece exit being approached by the tool. This observation is consistent with prior descriptions of the burr formation process, as plastic deformation of the hinge is first necessary for subsequent burr formation phases to occur. Therefore, it is expected that prediction of key burr parameters is likely possible based solely on in-situ characterized displacement fields and their analysis using the aforementioned methodology to determine the outermost point of the zone in which stress is equal to or greater than the flow stress.

As can be seen in Fig. 16, the location of the burr root changes significantly with cutting speed. At the same time, the (approximate) initial negative shear angle (β_0) is virtually identical for both conditions, with minor differences in the apparent slip-line morphology. The latter was estimated based on a line drawn normal to the observed vertical displacement fields' regions of constant displacement. Notably, the shape of the apparent slip-line qualitatively matches both the model-generated data and experimentally observed deformation field of both positive and negative burrs, with the latter notably failing along similar convex/radiused lines.

Since stress is proportional to displacement within the elastic limit, the data shown in Fig. 16a and b was further analyzed using the modified tractional Hertzian contact mechanics model described earlier. Fig. 16c and d represent overlays of the normalized (σ_{VM}/p_0) stress output of the model with the DIC-analyzed displacement fields. This model-informed analysis provides a visual illustration of the data summarized in Fig. 15b (i.e., the observed phenomenon that the stress at the burr root is at the flow stress of the workpiece material). Notably, based on the relative location of the burr root ahead of the cutting-edge and dozens of microns below the shear plane, the temperature at this point can be approximated to be nearly equal to the bulk workpiece temperature. Therefore, estimation of the workpiece flow stress can be reasonably undertaken based on room temperature values, rather than requiring complex constitutive analysis (e.g., via the Johnson-Cook or similar temperature/stress/strain-dependent model).

Rather than originating at the direct intersection of this contour of constant stress, the burr root is located on a slip-line, i.e., a 90-degree intersection with the von Mises stress field (σ_{VM}). It should be noted that the validity of the model is bounded by Saint-Venant's principle, which in this specific case implies that the modified Hertz model merely represents a reasonable and equivalent representation of the significantly more complex (true) surface load profile. Thus, model predictions can only be considered valid for distances greater than at least 20% of the half width of contact (depths greater than ~0.2a). For this reason, the model-predicted slip-lines in Fig. 16 are not drawn up to the surface and shear plane region, although it appears that some degree of extrapolation towards a perpendicular intersection with the shear plane may well be reasonably indicated.

Based on the experimental and analytical data shown in Figs. 15 and 16, a central finding of the present work can be summarized as follows: *The location of the burr root can be analytically determined based on the intersection of the slip-line originating from the middle of the shear plane and its intersection with the stress contour equal to the flow stress of the workpiece material.* This slip-line can be roughly approximated by the experimentally determined initial negative shear angle (β_0) but appears to exhibit a

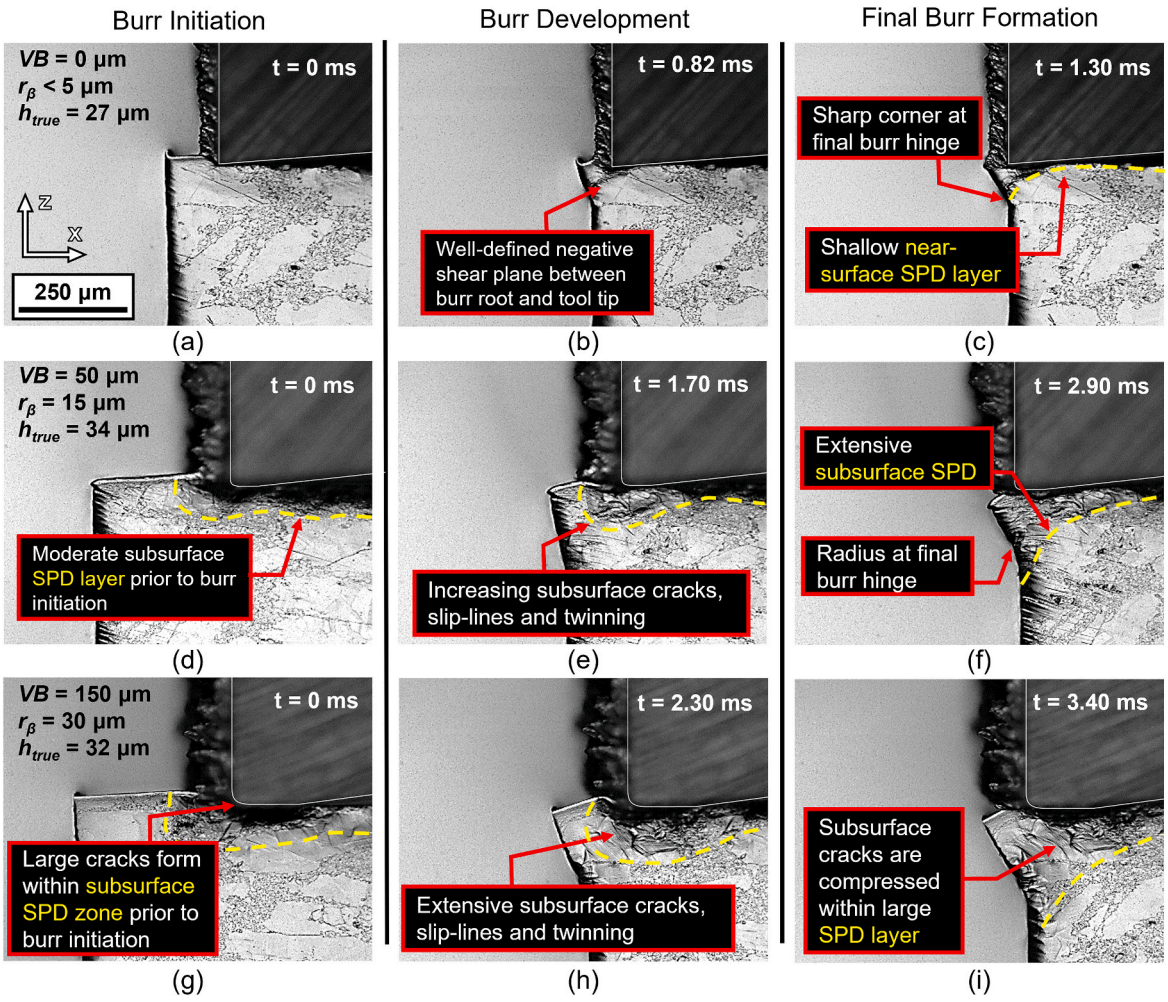

Fig. 19. Subsurface optical micrographs for (a–c) $VB = 0$; (d–f) $VB = 50$ µm; (g–i) $VB = 150$ µm at $v_c = 6$ m/min and $h = 40$ µm. Higher tool-wear resulted in increased near-surface SPD, which serves to both initiate and subsequently compress subsurface cracks. Negative shear is highly localized with sharp tools (b), allowing for negative burr formation with sufficiently large uncut chip thickness, while negative burr formation when cutting with worn tools is mostly suppressed due to subsurface SPD.

more complex morphology resulting from the state of stress in the workpiece subsurface because of the thermomechanical loads associated with a specific set of process parameters.

5. Analysis of exit burr fracture: The importance of microstructure and tool condition

Negative burrs describe the phenomenon under which a burr catastrophically separates (i.e., fractures) from the workpiece, leaving a chamfer, rather than a protrusion that characterizes the more common 'positive' burrs. Fig. 17 illustrates an event of negative burr fracture using in-situ imaging (the slow-motion footage of this experiment can also be viewed as Video 2 in the supplementary materials). Since they are rare, there has not been a clear description of what exactly causes negative exit burrs to form, and several authors have presented different possibilities. Hashimura et al. [41] suggested that the phenomenon is because of a ductile/brittle cutting mode—more ductile materials tend to generate larger (positive) burrs [16,42,43]. However, the exact conditions under which negative burrs occur in more brittle materials has not been systematically investigated.

Supplementary video related to this article can be found at https://doi.org/10.1016/j.ijmachtools.2023.104030

Most research describing negative burr formation has focused on the influence of cutting parameters. Iwata et al. [26] determined that negative burrs are attributed to the effective strain: if the effective strain is above a certain threshold, then fracture will occur along the negative shear zone and create a negative burr. Régnier et al. [33,44] found that uncut chip thickness has a significant effect on the development of negative burrs—higher uncut chip thickness results in a higher probability of negative burr formation, and the size of the negative burr would also increase with uncut chip thickness. Nakayama and Arai [14] discovered that higher uncut chip thickness, smaller tool rake angle, and lower cutting speed are favorable to exit burr fracture. However, this finding is contradicted by later studies, such as Régnier et al. [32], who observed the opposite effect with regard to rake angle: a negative rake angle almost never produced a negative burr, whereas a positive rake angle did under some conditions. However, it is important to note that these authors machined different materials: Nakayama and Arai [14] utilized 65-35 brass (which has a ductile cutting mode) and Régnier et al. [32] machined a cast aluminum alloy (which has a brittle cutting mode) in their study. Consequently, additional work is needed to help researchers and practitioners determine conditions under which negative burrs may be expected. The present study will present limited data for Inconel 718, as well as a proposed updated qualitative framework.

To further illustrate the stages of burr formation leading up to the fracture mechanism shown in Figs. 17 and 18 shows the corresponding DIC displacement fields. As previously displayed in Fig. 14, the intense deformation at the edge and negative shear plane can be seen. Fig. 18d

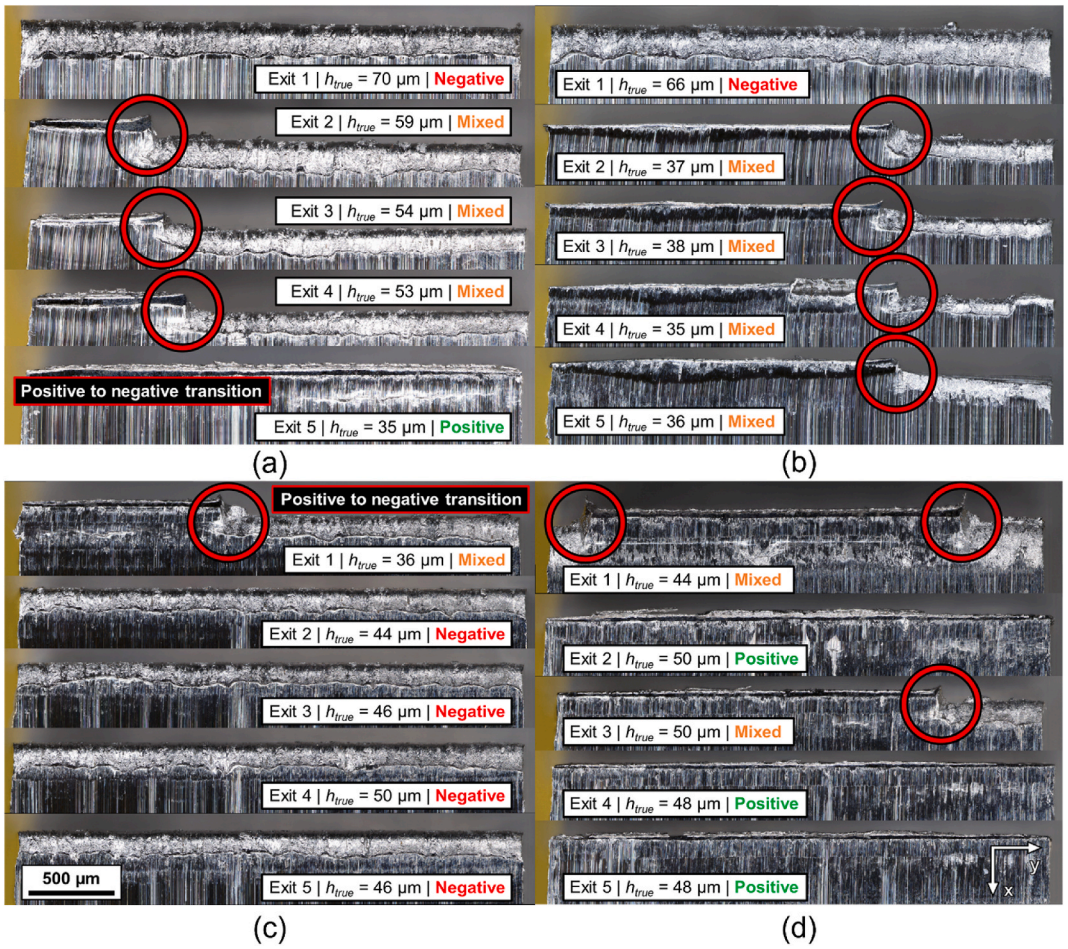

Fig. 20. Vertical view of positive to negative exit burr transition at $v_c = 60$ m/min, $h = 80$ µm for $VB = 0$: (a) Trial 1; (b) Trial 2 and for (c) $VB = 50$ µm; (d) $VB = 150$ µm. Partial burr fracture (highlighted by red circles) was observed and subsequently analyzed, showing strong correlation between the relative amount of fracture and the true (in-situ measured) uncut chip thickness at the time of burr initiation and formation at each exit. (For interpretation of the references to color in this figure legend, the reader is referred to the Web version of this article.)

shows how the SPD zone constrained around the PDZ is much bigger than the previous condition that had a much smaller uncut chip thickness in Fig. 14. Thus, both uncut chip thickness and wear serve to increase the degree of SPD around the PDZ. However, unlike with worn tools, sharp tools do not result in sufficient subsurface SPD to compress cracks once they are initiated; thus, under certain conditions, i.e., beyond a critical uncut chip thickness that allows for intergranular crack propagation, formation of a negative burr is possible with sharp tools. Moreover, Fig. 18f shows how during burr development, the most severe displacement occurs in the direction of the negative shear plane. Finally, Fig. 18h shows that following initiation, the shear transitions from being localized to the PDZ to occurring along the negative shear plane, further increasing the likelihood of crack propagation along this plane under proper alignment of microstructure and previously initiated cracks—Fig. 17 clearly demonstrates how the chip and fractured burr separate along the negative shear plane, which aligns with a region of smaller grains that allow for intergranular crack propagation even after a lager crack becomes blunted in the transgranular regime (see Fig. 17a and b).

Past research has presented many plausible causes for the formation of negative burrs (material ductility, rake angle, strain, etc.), but the present work has revealed strong evidence that they are caused by three main factors: (i) strain rate, (ii) a geometric size effect of the uncut chip thickness, and (iii) intergranular fracture along the boundaries of grain colonies. Additionally, findings point to the existence of a critical uncut chip thickness (h_{crit}) for negative exit burr formation for a given cutting speed condition, based on two major factors.

Firstly, the strain rate was identified as a relevant parameter because no negative burrs were obtained for identical conditions across a wide range of uncut chip thickness and tool-wear values at the lower cutting speed of 6 m/min—burrs only formed at the high cutting speed of 60 m/min. This difference can be observed qualitatively when comparing the footage of these conditions: Video 3 (low cutting speed) and Video 4 (high cutting speed) in the supplementary materials. Secondly, a microstructural size effect indicating a critical uncut chip thickness is present because negative burrs only formed at larger values of true uncut chip thickness (h_{true}).

Supplementary video related to this article can be found at https://doi.org/10.1016/j.ijmachtools.2023.104030

Notably, while chip formation and burr formation with sharp tools was found to occur via well-defined, approximately linear positive and then negative shear planes, respectively, the intense mechanical loads imposed by worn tools resulted in subsurface cracks that originated from the primary shear plane. Moreover, extensive twin boundaries and slip-lines occurred within the SPD layer beneath the worn tools, further illustrating the extent and degree of plastic deformation induced with worn tools, as was shown in Fig. 14. Although worn tools resulted in brittle subsurface cracking, their simultaneous plastic deformation of an increasingly large subsurface SPD layer plastically deformed such cracks by the time the tool would pass completely over a given subsurface crack. While evidence of the previously initiated cracks remained in the final machined subsurface, including the material comprising the final

burr, cracks were compressed prior to propagating or coalescing. Consequently, worn tools effectively suppressed negative/brittle burr formation due to severe plastic deformation. Nevertheless, the remaining compressed cracks should be considered significant machining-induced damage and are expected to negatively impact both ductility and fatigue performance of components machined in this manner. Therefore, determination of crack-free machining regimes for life-limited components, such as turbine blades, should be explored further by future studies that may build on this investigation. In this context, this study clearly shows that cracking initiated in both inter and transgranular regimes, but cracks rapidly blunted in the transgranular regime. Based on the bimodal microstructure of the Inconel 718 workpiece used in the present study, this implied that for a crack to propagate, a path between the large γ (Ni-FCC, appearing white) grains and the much smaller precipitate-strengthened fine-grained colonies is required. Thus, a microstructural size effect between the uncut chip thickness, microstructure, and tool-wear condition naturally emerges, to be discussed in Section 5.1.

5.1. Statistical analysis of microstructural size effect for negative burr formation

A higher uncut chip thickness is more likely to cause negative burrs because the shear zone ahead of the cutting area is in tension, as opposed to the compression shear zone at low uncut chip thickness [45]. Thus, a shear zone in compression requires much higher strain for fracture than a shear-zone in tension [33]. For this observed size effect, microstructure was determined to play a central role based on in-situ observations such as those shown in Fig. 17. Specifically, fracture during negative burr formation was typically intergranular, along the boundaries between grain colonies (clusters of grains, see Fig. 17). This observation is reasonable, given that transgranular fracture typically requires significantly more energy because it would entail yielding of the grain matrix itself, rather than fracturing along the significantly more brittle grain boundary region.

High-resolution images from a comparison of the negative exit burrs for different tool conditions are shown visually in Fig. 20. The corresponding footage of the cuts for the first two exits can also be viewed as Videos 4-7 in the supplementary materials. As can be seen, there was zero fracture at $h_{true} = 35$ µm, partial fracture between $h_{true} = 53$–59 µm, and complete fracture at $h_{true} = 70$ µm for the sharp tool in Fig. 20a. The conditions for this experiment were repeated and the same pattern was observed in Fig. 20b; the true uncut chip thickness was considerably smaller for Exits 2–4 than Trial 1, and the transition likewise shifted to the right, resulting in a smaller partial negative burr. Additionally, the point of transition along the width of the workpiece was very similar when values of h_{true} were close, indicating a definite relationship. The percentage of negative burr formation for each edge across both trials is plotted in Fig. 21, where the degree of negative burr formation exhibits a linear relationship. The regression indicates that partial fracture will occur at a $h_{true} > 20$ µm. After reviewing the results at the lower programmed uncut chip thicknesses (10 µm, 20 µm, 40 µm, where there was no fracture), this is indeed the case, as none of the values of h_{true} were above 20 µm. Correspondingly, partial fracture begins when the exit burr thickness is above $b_t > 80$ µm.

Supplementary video related to this article can be found at https://doi.org/10.1016/j.ijmachtools.2023.104030

Fig. 20c and d shows the negative burrs obtained with worn tools, and there are some notable differences compared to the sharp tools. Firstly, for $VB = 50$ µm, there was partial fracture at $h_{true} = 36$ µm, but complete fracture at $h_{true} = 44$–50 µm, indicating that h_{crit} falls between 36 and 44 µm. For $VB = 150$ µm, no full negative burrs were observed as there was very little fracture. Minimal fracture was seen at $h_{true} = 44$ µm and $h_{true} = 50$ µm, but the remaining exits produced full positive burrs despite h_{true} being 48–50 µm. Additionally, the first exit yielded fracture at both ends of the workpiece, rather than only on the right side such as in all other remaining cases. Thus, this suggests that in addition to the strain rate (i.e., cutting speed), geometric size effect (i.e., true uncut chip

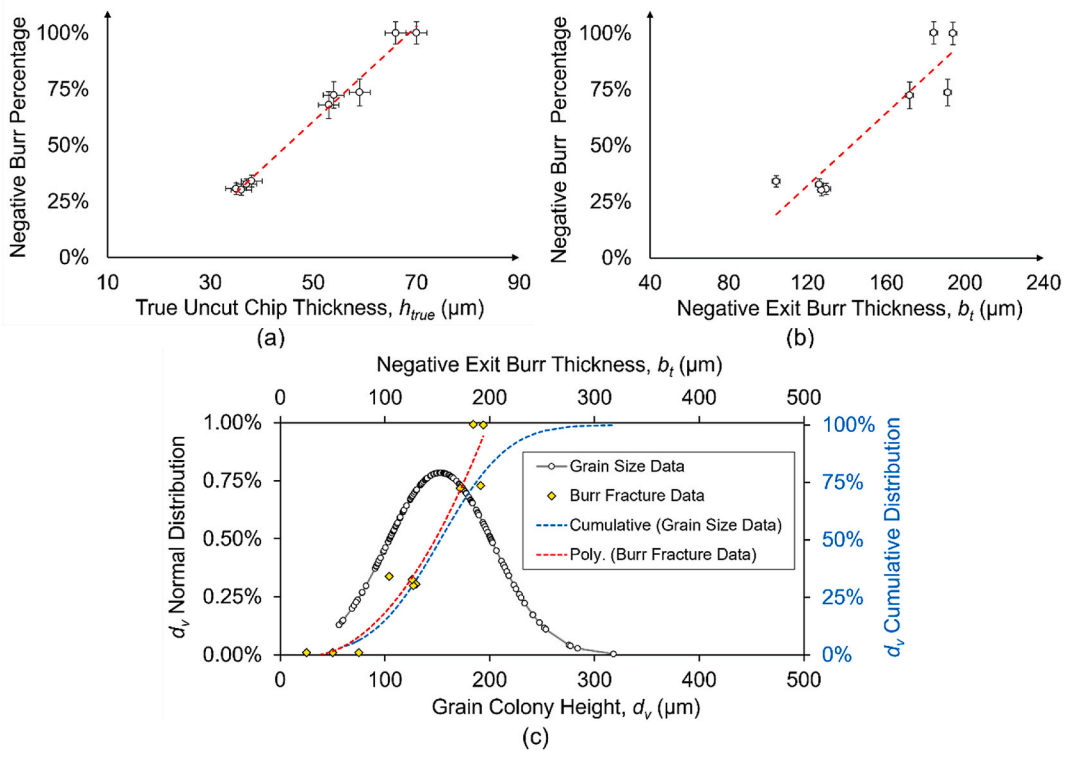

Fig. 21. Negative burr formation development at $VB = 0$ µm, $v_c = 60$ m/min, $h = 80$ µm with (a) true uncut chip thickness (h_{true}) and (b) burr thickness (b_t); (c) relationship between negative burr fracture and grain size, as illustrated with the stochastic (normal) distribution of grain colony height and burr fracture percentage. Results indicate a clear microstructural size effect between the grain colony height and the negative burr exit thickness.

thickness), and microstructural size effect (i.e., intergranular fracture), the critical uncut chip thickness is also dependent on tool-wear. While a definitive trend cannot be extracted from the very limited data points, it can be inferred that the relationship between tool-wear and the critical uncut chip thickness for negative burrs is likely nonlinear since at $VB = 50$ μm the threshold was much lower than at $VB = 0$ μm, however it rises significantly again at $VB = 150$ μm. Determining not only the exact value for h_{crit} but also the correlation with tool-wear was deemed outside of the scope of this study but will be of great interest in future work.

Generally, a finer grain distribution results in a higher grain boundary to volume ratio: this improves the strength of the material, increasing its resistance to bulk deformation (e.g., Hall Petch hardening) [46]. Thus, machining a sample with smaller grains will also yield higher cutting forces [46]. However, when the stress field is highly localized, larger grains increase the likelihood that a crack will propagate through a grain rather than along its boundary. Evidence from this study shows that cracks become blunted in the transgranular regime, and so larger grains may therefore serve to effectively increase fracture toughness for deformation at the grain scale (i.e., finish machining). To further investigate the microstructural effect, the statistical distribution of the heights of the grain colonies in the bimodal workpiece were measured across the sample and plotted alongside the burr fracture data in Fig. 21c. As can be seen, the cumulative distribution grain colony height coincides with the negative exit burr thickness, confirming the presence of intergranular cracking.

Based on in-situ observations, as well as detailed statistical analysis of various microstructural features and burr metrics, it is hypothesized that 100% exit burr fracture occurs whenever the exit burr thickness (i.e., the depth to which the subsurface plastic zone, bounded by the negative shear angle and associated slip-line), is contained within a grain colony. Below this critical value, which for the investigated microstructure of Inconel 718 resulted in the critical uncut chip thickness being approximately equal to 21 μm, along with the corresponding critical burr thickness (i.e., the depth of the slip-line below the surface at burr initiation) of approximately 80 μm (see Fig. 21a and b). Below this value, no fracture occurred, as only a subset of grain colonies was smaller than the actual burr thickness. The cumulative fracture percentage and cumulative percentage of grains of a given colony height correlated closely, as shown in Fig. 21c. Notably, the correlation between microstructural features, and associated fracture mechanics (specifically, intergranular fracture requiring lower energy than transgranular fracture) implies that a chemically identical material (e.g., Inconel 718 with different heat treatment) would exhibit a different threshold for exit burr fracture depending on its microstructure. Thus, this is a novel finding not previously documented by other researchers. Further, given the bimodal microstructure of this Inconel 718 workpiece in this treated condition, it may be reasonable to assume that this sample facilitated fracture because of the long grain boundaries due to the previously discussed grain colonies. The only other work to investigate burr formation with respect to microstructure using in-situ techniques is Wu et al. [46]. However, they only assessed side burr formation, where they observed that side burr size increased with grain size. Future work will be required to fully elucidate and eventually predict the influence of microstructure on negative burr formation. This will require testing of workpieces at different heat treatments and grain sizes.

In addition to the statistical evidence presented in Fig. 21c and laid out in the preceding discussion, in-situ observations, and a reasonable physical mechanism (specifically greater stress intensity with sharp tools and greater uncut chip thickness), as well as increased strain rate at higher cutting speed, further support the hypothesis that negative burr formation requires (i) high cutting speed, (ii) a certain critical uncut chip thickness, and (iii) sharp tools. The observed lack of negative burrs with worn tools may be readily explained by the in-situ data shown in Figs. 12, 14 and 18. Specifically, the increased degree of plastic deformation or ploughing with worn tools serves to suppress crack growth, even as crack initiation is increased when cutting with worn tools. Since cracks cannot grow sufficiently to result in complete burr fracture (i.e., a negative burr), worn tools merely leave partially fractured burrs that may nevertheless present major stress risers. Sharp tools do not induce sufficient ploughing to compress cracks once they are formed at high speed and beyond a critical chip thickness that occurs when the negative shear zone passes between two large grains, and so complete negative burr formation is statistically guaranteed beyond this critical uncut chip thickness, and partially possible at lower values of h. The present study provides strong evidence that crack formation and propagation (or suppression) mechanisms are at play during burr formation in Inconel 718.

6. Conclusions

This paper presented a fundamental study of burr formation in Inconel 718 under finish-machining conditions. Results show that burr formation can be heavily influenced by the level of tool-wear and control of cutting parameters—numerous profiles for exit burr characteristics were generated and the key relationships are as follows.

- This study provides new insights into the relationships between the workpiece material's microstructure, machining parameters, and tool condition on both crack formation and propagation/plasticity during burr formation.
- As expected, burr size (b_t and b_h) always increased with true uncut chip thickness. Tool-wear only had a significant effect on burr size at low cutting speed ($v_c = 6$ m/min) and only for b_t. This is believed to be due to cold work and strain hardening associated with machining at low speeds with worn tools. This effect of tool-wear is a new insight not previously reported by other researchers.
- Uncut chip thickness had a minor effect on the inclination angle (ψ), with tool condition and cutting speed having no significant influence. This study is perhaps the first to consider how the inclination angle changes with varying cutting parameters.
- The apparent exit burr initiation distance (ω) increased with tool-wear, indicating that the transition from steady-state chip formation to burr formation begins earlier for worn tools—this is attributed to higher mechanical stress ahead of the tool, as was shown from DIC displacement fields. Interestingly, ω was found to be higher at low cutting speed, likely because of increased strain hardening. The initiation distance of course increased steadily with uncut chip thickness. However, where previous works only assessed the sensitivity of ω with respect to uncut chip thickness and rake angle, the present work also introduced the effect of tool-wear.
- The initial negative shear angle (β_0) for exit burrs was found to be independent of all conditions. No other study has considered the influence of tool wear on this parameter. The newly identified exit burr initiation angle (η) was constant with respect to the different conditions. This angle was previously never reported in the literature, so this is a significant discovery as it is key for measuring numerous burr metrics.
- DIC analysis showed that worn tools induced a much larger mechanical stress field in the subsurface, which in turn leads to a higher exit burr initiation distance. Similarly, worn tools also resulted in much more severe deformation along the workpiece edge.

An analysis was carried out to quantify the displacement and stress at the root of exit burr formation using a semi-analytical approach. No other study has managed to employ DIC for the purpose of analyzing burr formation to this extent. This work is the first to calculate the displacement and stress present at the exit burr root during deformation, where the following conclusions were drawn.

- It was found that the average displacement at the exit burr root was 1.45 μm, with no observed trend between the control parameters of uncut chip thickness, tool-wear, and cutting speed.

- Results show that the normalized stress at the exit burr root is equal to approximately 98% of the flow stress. This reveals that exit burr development begins when the edge of the workpiece intersects the contour corresponding to the flow stress. It was also found that the burr root falls on the intersection between the slip-line and the contour line.

It is well known that exit burrs tend to fracture at a certain point, forming a 'negative breakout'. This phenomenon has only been lightly explored in previous works, with only a select number of studies presenting possible causes for fracture to occur. The present work is the first to not only provide a deep look at this mechanism, but also shed light on the influence of three major cutting parameters. From the conditions in this study, it is believed that negative exit burrs are driven by the following factors.

- Negative exit burrs occur at a certain threshold for strain rate, uncut chip thickness, grain size, and tool condition. The strain rate was confirmed to be the most deciding factor as for cases where all other conditions remained the same, no negative burrs formed at low cutting speed, only high cutting speed. Moreover, there was also observed to be a critical uncut chip thickness for negative burr formation for a given cutting speed—anything below this amount resulted in partial fracture. Finally, the fracture behavior with worn tools differed greatly than with sharp tools.
- Greater mechanical loading of the workpiece due to increased uncut chip thickness and tool-wear was observed to result in greater likelihood of crack initiation. However, worn tools also generate larger subsurface plastic deformation, so negative/fractured burrs occurred only with sharp tools at increased feed rates.
- Through measurement of grain colony size, it was determined that there was a strong correlation with the negative exit burr thickness, lending evidence to intergranular fracture. Thus, there is reason to believe that complete fracture occurs whenever the negative burr thickness is contained within a grain colony. This corresponded to a critical uncut chip thickness and exit burr thickness of 20 μm and 80 μm, respectively, above which there is fracture.

In summary, this manuscript addressed several aspects pertaining to burr formation: the change in geometry/size, the strains/stresses in the subsurface during exit burr development, and the mechanism behind exit burr fracture. While all three of these categories were greatly expanded upon, there is still potential for future research to refine the findings of this study even further. For instance, this study presented illuminating new insights on the exit burr formation mechanism, particular with regards to microstructure, which has been very scarcely explored in the current state of the art. However, there is still a wide array of conditions surrounding exit burr fracture that could not be comprehensively included in the present work. Determining the exact onset of fracture for different settings of strain rate, feed, and microstructure will be necessary for future researchers studying burr formation.

Supplementary data to this article can be found online at https://doi.org/10.1016/j.ijmachtools.2023.104030.

Credit author statement

Hamzah Zannoun: Conceptualization, Methodology, Validation, Formal analysis, Investigation, Writing – Original Draft, Writing – Review & Editing, Visualization **Julius Schoop**: Conceptualization, Methodology, Formal analysis, Resources, Writing - Original Draft, Writing - Review & Editing, Visualization, Supervision, Funding acquisition

Declaration of competing interest

The authors declare that they have no known competing financial interests or personal relationships that could have appeared to influence the work reported in this paper.

Data availability

Data will be made available on request.

Acknowledgments

This work was supported by the U.S. National Science Foundation, grant number 2143806, project title "CAREER: Thermomechanical Response and Fatigue Performance of Surface Layers Engineered by Finish Machining: In-situ Characterization and Digital Process Twin".

References

[1] S.Y. Jin, A. Pramanik, A.K. Basak, C. Prakash, S. Shankar, S. Debnath, Burr formation and its treatments—a review, Int. J. Adv. Manuf. Technol. 107 (2020) 2189–2210.
[2] P.J. Arrazola, Assessment of Deburring Costs in Industrial Case Studies, in: CIRP International Conference on Burrs, Springer, Kaiserslautern, Germany, 2009.
[3] J. Leopold, R. Wohlgemuth, Modeling and Simulation of Burr Formation: State-of-the-Art and Future Trends, in: CIRP International Conference on Burrs, Springer, Kaiserslautern, Germany, 2009.
[4] L.K. Gillespie, The Formation and Properties of Machining Burrs, Utah State University, 1973.
[5] C. Legrand, G. Fromentin, G. Poulachon, M. Rancic, Development of an enhanced burr accumulation model during orthogonal cutting of nickel-based super alloy, Int. J. Adv. Manuf. Technol. 123 (2022) 331–343.
[6] K. Lee, D.A. Dornfeld, Micro-burr formation and minimization through process control, Precis. Eng. 29 (2005) 246–252.
[7] A. Muhammad, M.K. Gupta, T. Mikołajczyk, D.Y. Pimenov, K. Giasin, Effect of Tool Coating and Cutting Parameters on Surface Roughness and Burr Formation during Micromilling of Inconel 718, Metals 11 (2021) 167.
[8] K. Aslantas, A. Çiçek, The effects of cooling/lubrication techniques on cutting performance in micro-milling of Inconel 718 superalloy, Procedia CIRP 77 (2018) 70–73.
[9] X. Wu, L. Li, N. He, Investigation on the burr formation mechanism in micro cutting, Precis. Eng. 47 (2017) 191–196.
[10] M.C. Avila, D.A. Dornfeld, On the Face Milling Burr Formation Mechanisms and Minimization Strategies at High Tool Engagement, 2004.
[11] G.-L. Chern, D.A. Dornfeld, Burr/Breakout Model Development and Experimental Verification, J. Eng. Mater. Technol. 118 (1996) 201–206.
[12] M. Bakkal, A.J. Shih, S.B. McSpadden, C.T. Liu, R.O. Scattergood, Light emission, chip morphology, and burr formation in drilling the bulk metallic glass, Int. J. Mach. Tool Manufact. 45 (2005) 741–752.
[13] S.-L. Ko, D.A. Dornfeld, A Study on Burr Formation Mechanism, J. Eng. Mater. Technol. 113 (1991) 75–87.
[14] K. Nakayama, M. Arai, Burr Formation in Metal Cutting, CIRP Annals 36 (1987) 33–36.
[15] D. Dornfeld, S. Min, in: A Review of Burr Formation in Machining, CIRP International Conference on Burrs, Springer, Kaiserslautern, Germany, 2009.
[16] J.C. Aurich, D. Dornfeld, P.J. Arrazola, V. Franke, L. Leitz, S. Min, Burrs—Analysis, control and removal, CIRP Ann. 58 (2009) 519–542.
[17] S. Cedergren, S. Olovsjö, G. Sjöberg, L. Nyborg, The effects of grain size and feed rate on notch wear and burr formation in wrought Alloy 718, Int. J. Adv. Manuf. Technol. 67 (2013) 1501–1507.
[18] F. Vollertsen, Categories of size effects, J. Inst. Eng. Prod. 2 (2008) 377–383.
[19] L. Pilný, L. De Chiffre, M. Píška, M.F. Villumsen, Hole quality and burr reduction in drilling aluminium sheets, CIRP Journal of Manufacturing Science and Technology 5 (2012) 102–107.
[20] D. Biermann, M. Steiner, Analysis of Micro Burr Formation in Austenitic Stainless Steel X5CrNi18-10, Procedia CIRP 3 (2012) 97–102.
[21] A. De Bartolomeis, S.T. Newman, I.S. Jawahir, D. Biermann, A. Shokrani, Future research directions in the machining of Inconel 718, J. Mater. Process. Technol. 297 (2021), 117260.
[22] D.d. Oliveira, M.C. Gomes, M.B.d. Silva, Influence of cutting fluid application frequency on the surface quality of micromilled slots on Inconel 718 alloy, Procedia Manuf. 48 (2020) 553–558.
[23] J. Blaber, B. Adair, A. Antoniou, Ncorr: Open-Source 2D Digital Image Correlation Matlab Software, Exp. Mech. 55 (2015) 1105–1122.
[24] T.S. Nisbet, G.W. Mullett, Rolling Bearings in Service, Interpretation of Types of Damage, 1978.
[25] A.J. Pekelharing, The exit failure in interrupted cutting, CIRP Annals 27 (1983).
[26] K. Iwata, K. Ueda, K. Okuda, Study of Mechanism of Burrs Formation in Cutting Based on Direct SEM Observation, J. Jpn. Soc. Precis. Eng. 48 (1982) 510–515.

[27] F. Schäfer, F. Breuninger, H. Sauer, B. Schuh, W. Seyderhelm, H.J. Winter, H. J. Warnecke, H.U. Brauner, Deburring: Theory, Processes, Systems, Krausskopf, 1975.
[28] A. Rangarajan, OPTIMIZATION OF FACE MILLING PROCESS - TOOL PATH AND PROCESS PLANNING TECHNIQUES, University of California, Berkeley, 2005.
[29] A.M. De Souza, W.F. Sales, E.O. Ezugwu, J. Bonney, A.R. Machado, Burr formation in face milling of cast iron with different milling cutter systems, Proc. IME B J. Eng. Manufact. 217 (2003) 1589–1596.
[30] G.C. Wang, C.Y. Zhang, Study on the Forming Mechanism of the Cutting-direction Burr in Metal Cutting, Key Eng. Mater. 259–260 (2004) 868.
[31] O. Olvera, G. Barrow, Influence of exit angle and tool nose geometry on burr formation in face milling operations, Proc. IME B J. Eng. Manufact. 212 (1998) 59–72.
[32] T. Régnier, B. Marcon, J. Outeiro, G. Fromentin, A. D'Acunto, A. Crolet, Investigations on exit burr formation mechanisms based on digital image correlation and numerical modeling, Mach. Sci. Technol. 23 (2019) 925–950.
[33] T. Régnier, G. Fromentin, B. Marcon, J. Outeiro, A. D'Acunto, A. Crolet, T. Grunder, Fundamental study of exit burr formation mechanisms during orthogonal cutting of AlSi aluminium alloy, J. Mater. Process. Technol. 257 (2018) 112–122.
[34] P. Hofman, I. Kvasnicka, Analytical Model for Burr Formation During Orthogonal Machining and its Verification, 6th International Conference Precision Surface Finishing and Deburring Technology, St. Petersburg, Russia, 2000.
[35] M. Hashimura, J. Hassamontr, D.A. Dornfeld, Effect of In-Plane Exit Angle and Rake Angles on Burr Height and Thickness in Face Milling Operation, J. Manuf. Sci. Eng. 121 (1999) 13–19.
[36] A.A. Toropov, S.L. Ko, J.M. Lee, A New Burr Formation Model for Orthogonal Cutting of Ductile Materials, CIRP Ann. 55 (2006) 55–58.
[37] T. Platt, A. Meijer, D. Biermann, Conduction-Based Thermally Assisted Micromilling Process for Cutting Difficult-to-Machine Materials, J. Mater. Process. Manuf. Sci. 4 (2020) 34.
[38] J. Schoop, M.M. Hasan, H. Zannoun, Physics-Informed and Data-Driven Prediction of Residual Stress in Three-Dimensional Machining, Exp. Mech. 62 (2022) 1–14.
[39] R.J. Pomeroy, K.L. Johnson, Residual stresses in rolling contact, J. Strain Anal. 4 (1969) 208–218.
[40] A.M. Group, J.E. Merwin, K.L. Johnson, An Analysis of Plastic Deformation in Rolling Contact, Proc. Inst. Mech. Eng. 177 (1963) 676–690.
[41] M. Hashimura, Y.P. Chang, D. Dornfeld, Analysis of Burr Formation Mechanism in Orthogonal Cutting, J. Manuf. Sci. Eng. 121 (1999) 1–7.
[42] J. Kim, D.A. Dornfeld, Development of an Analytical Model for Drilling Burr Formation in Ductile Materials, J. Eng. Mater. Technol. 124 (2002) 192–198.
[43] J. Ahn, H. Lim, Side Burr Generation Model in Micro-Grooving, in: 12th Annual Meeting of the American Society for Precision Engineering, American Society for Precision Engineering, Raleigh, NC, 1997.
[44] T. Régnier, G. Fromentin, A. D'Acunto, J. Outeiro, B. Marcon, A. Crolet, Phenomenological Study of Multivariable Effects on Exit Burr Criteria During Orthogonal Cutting of AlSi Alloys Using Principal Components Analysis, J. Manuf. Sci. Eng. 140 (2018), 101006.
[45] Y.M. Abushawashi, Modeling of Metal Cutting as Purposeful Fracture of Work Material, Michigan State University, 2013.
[46] X. Wu, L. Li, N. He, M. Zhao, Z. Zhan, Investigation on the influence of material microstructure on cutting force and bur formation in the micro cutting of copper, Int. J. Adv. Manuf. Technol. 79 (2015) 321–327.